Pontifícia Universidade Católica
do Rio de Janeiro

André do Nascimento Barbosa

Tungsten disulfide: new approaches for characterization and surface modification

Tese de Doutorado

Thesis presented to the Programa de Pós-graduação em Física of PUC-Rio in partial fulfillment of the requirements for the degree of Doutor em Ciências - Física.

Advisor: Fernando Lázaro Freire Júnior

Rio de Janeiro

November 2020

Pontifícia Universidade Católica
do Rio de Janeiro

André do Nascimento Barbosa

Tungsten disulfide: new approaches for characterization and surface modification

Thesis presented to the Programa de Pós-graduação em Física of PUC-Rio in partial fulfillment of the requirements for the degree of Doutor em Ciências - Física. Approved by the examination committee:

Prof. Fernando Lázaro Freire Júnior
Advisor
Departmento de Física – PUC-Rio

Prof. Marco Cremona
Departmento de Física – PUC-Rio

Prof. Rodrigo Gribel Lacerda
UFMG

Prof. Gino Mariotto
UNIVR

Prof. Daniel Lorscheitter Baptista
UFRGS

Rio de Janeiro, November 30th, 2020.

André do Nascimento Barbosa

Obtained his bachelor's degree in physics at UERJ (Universidade do Estado do Rio de Janeiro) in 2015.

Ficha Catalográfica

Barbosa, André do Nascimento Barbosa

Tungsten disulfide: new approaches for characterization and surface modification/ André do Nascimento Barbosa; Advisor: Fernando Lázaro Freire Júnior. – 2020.

86 f.: il. color. ; 30 cm

Tese (Doutorado)–Pontifícia Universidade Católica do Rio de Janeiro, Departamento de Física, 2020.

Inclui referências bibliográficas.

1. Física – Teses. 2. Dicalcogenetos de metais de transição 3. transição de gap de banda indireta para direta 4. modificação estrutural.. I.
Freire Jr, Fernando L. II. Pontifícia Universidade Católica do Rio de Janeiro. Departamento de Física. III. Título.

CDD: 004

To Alcina, Renata and Aline

In memory of Antônio Barbosa

Acknowledgments

This study was financed in part by the Coordenação de Aperfeiçoamento de Pessoal de Nível Superior - Brasil (CAPES) - Finance Code 001; CAPES-Print-88887.368479/2019-00 and the University of Verona within the CooperInt-2019 program. Also, my fellowship was financed by Conselho Nacional de Desenvolvimento Científico e tecnológico (CNPq) (CNPq - 140077/2017-0).

I would like to thank Professor Fernando Lázaro for being, in some ways, someone that believed I could go a little bit further.

I thank professors Gino Mariotto and Maurício Terrones's contributions and opportunities abroad.

Also, I would like to thank Professor Marcelo Maia da Costa for introducing the lab, discussions, and suggestions.

I thank Dr. Cesar Diaz Mendoza, Dr. Neileth Stand Figueroa for collaborating with XPS and AFM measurements.

I cannot forget, Dr. Felipe Ptak Lemos, Dr. Suellen Tozzetti, and all the technical support staff and collaborators, especially Giza.

I also had good support from my colleagues and friends, especially Dr. Gil Capote Mastrapa, Dr. Eric Cardona Romani, Professor Cecilia Vilani, and fellow students Shuai Zhang and Syed Hamza.

Moreover, I thank all the support from all other people that, in some way, helped me.

Of course, I would like to thank my family: My sister Renata Barbosa, my mother Alcina Nascimento, my father Antônio Barbosa, and aunt Odineia Silva. I am what I am because of you. Also, I cannot forget Uncle Carley and aunt Sônia, that, although not family, helped my mother and encouraged my education abroad.

Finally, Aline Mazzarella. I am confident that without you, I simply would give up. I love you.

Abstract

André do Nascimento Barbosa; Fernando Lázaro Freire Júnior (Advisor) . **Tungsten disulfide: new approaches for characterization and surface modification.** Rio de Janeiro, 2020, 86p. Tese de doutorado - Departamento de física, Pontifícia Universidade Católica do Rio de Janeiro.

Transition metal dichalcogenides, such as molybdenum disulfide, tungsten disulfide, and others exhibit many interesting properties. Such properties make them good prospects for future applications, especially in optoelectronics. From telecommunication to medicine, due to the interesting indirect-to-direct band-gap transition, one isolates a single layer of the material. One of the goals of this thesis is to modify the structure of tungsten disulfide using a simple, reliable, structural modification approach, i.e., plasma treatment. In this way, we were able to enhance the materials' luminescence emission intensity up to 34%. Also, this treatment p-doped the monolayer structures, opening doors for the realization of devices. Another objective of this work is to develop new ways to characterize this material, particularly the determination of a critical parameter for WS_2 applications, the number of layers, using Raman spectroscopy, where we developed a efficient method to discriminate monolayers independently of induced strain, structure modification and doping.

Keywords:

transition metal dichalcogenides, indirect-to-direct band-gap transition, structural modification.

Resumo

André do Nascimento Barbosa; Fernando Lázaro Freire Júnior. **Dissulfeto de Tungstenio: novas formas de caracterização e modificação de superfície.** Rio de Janeiro, 2020, 86p. df de Doutorado - Departamento de Física, Pontifícia Universidade Católica do Rio de Janeiro.

Dicalcogenetos de metais de transição, como dissulfeto de molibdênio, disseleneto de tungstênio, entre outros exibem muitas propriedades interessantes que fazem os materiais desta família boas perspectivas para aplicações futuras, especialmente em diversas applicações da optoeletrônica, desde telecomunicações até medicina, devido à interessante transição de gap de banda indireta para direta que ocorre quando se isola uma única camada destes materiais. Um dos objetivos desta tese é: explorando essa propriedade e modificando a estrutura da dissulfeto de tungstênio usando um método simples e confiável de modificação estrutural, pode-se aprimorar as propriedades dos materiais de forma eficiente, bem como desenvolver novas maneiras de caracterizar esse material e suas modificações, em particular, a determinação de um parâmetro chave para aplicações de WS_2, o número de camadas, usando espectroscopia Raman. Neste caso, o tratamento de plasma melhorou a intensidade de fotoemissão em 34% além de p-dopar os cristais monocamada, abrindo portas para a realização de dispositivos baseados em WS_2. Além disso, desenvolvemos um método de discriminação de monocamadas que é independente de tensão aplicada, modificação strutural ou dopagem.

Palavras-chave:

Dicalcogenetos de metais de transição, transição de gap de banda indireta para direta, modificação estrutural.

Index

List of figures

List of tables

"Criar o que não existe ainda deve ser a pretensão de todo sujeito que está vivo"

Paulo Freire

1
Introduction

1.1
A Brief Introduction to 2D transition metal dichalcogenides

2D transition metal dichalcogenides (TMDs) are materials with interesting properties with many future applications [1-2]. These materials, especially MoS_2 and WS_2, have unique optical behavior and, alongside graphene, continues to push interest in the investigation and research on 2D materials [3-5]. Although the theoretical and experimental knowledge on such materials, there is plenty of room regarding research in applied and fundamental science.

Like graphene, one can easily exfoliate these materials due to the weak Van der Waals inter-layer interaction [6, 7]. WS_2, which is a pile 3-atom thick, with tungsten atom layers sandwiched between two planes of sulfur atoms, is a semiconducting material, which properties are important for electronic device applications. A remarkable property of WS_2, like some other TMDs, is the indirect-to-direct bandgap transition which occurs when one isolates a single 3-atom layer from the bulk crystals [8-10].

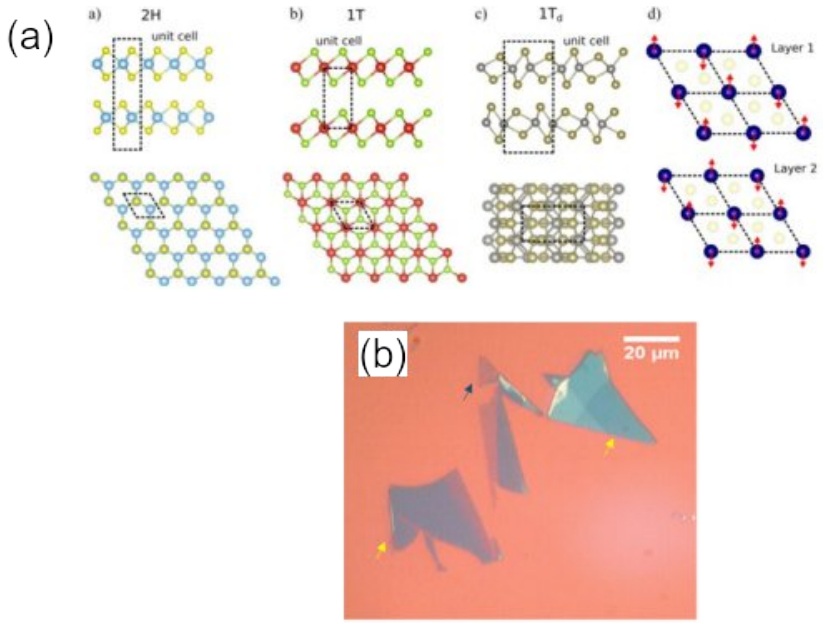

Figure 1.1. (a) A scheme of the layered characteristic of TMDs. (b) Exfoliated WS_2 layers on a SiO_2 substrate. [1]

Bulk WS_2 has an indirect bandgap of circa 1.4 eV, and the isolated monolayer shows a direct bandgap of 1.9 eV [11,12]. Although mechanically exfoliated WS_2 yields almost defect-free monolayers, such a process is impracticable for future industrial implementation. However, chemical vapor deposition (CVD) comes as one of the manufacturing possibilities that can produce large-high-quality monolayer flakes. It is more reliable than other means when quality, thickness, and flake size are important parameters [13-16].

The ability to manufacture monolayers reliably at large scales essentially creates a need to standardize the physical properties of pristine TMD materials, and by doing so, one may modify the structure through several different methods and tune the properties of the material to its needs in a large number of structures at once. One of these approaches is the low-energy surface plasma treatment [17,18]. In previous studies regarding MoS_2 monolayers, it was shown that cold plasma treatment might be used to control the photoemission intensity [19-21]. These works demonstrated that oxygen incorporation either significantly improved or quenched the luminescence intensity due to chemical modification of the material or doping.

Moreover, a similar straightforward N-plasma treatment was used to enhance the field-effect transistor electron mobility and decrease the threshold voltage of the device [22]. Also, as these methods are performed at many samples at once, a statistical study involving many samples is needed, so that the average final effect is considered. This average behavior of the treated crystals gives the correct picture of the plasma treatment effect. Such a process is essentially an ion bombardment of the sample where defects and atomic substitutions are incorporated rather randomly.

In a recent study, Ga^+ irradiation on WS_2 was used to study the photoluminescence (PL) response as a function of the ion dose. It was shown that the PL was overly sensitive to it [23]. In this case, the PL signal of monolayer WS_2 was quenched because of the treatment. These works are examples of how one may effectively modify the properties of 2D materials through means of ion irradiation for either defect creation or substitutional doping.

Photodiodes and light-emitting devices are among the most important application areas for future TMD-based devices used as primary emission or absorption materials. These applications are based on the indirect-to-direct bandgap transition that allows for a much-increased radiative recombination

probability amplitude [24].

Moreover, MoS_2 and WS_2 monolayers exhibit unintentional n-doping, motivating an intense search to achieve a stable conversion to p-type doping, since it is necessary for their use in the next generation of p-n junction-based optoelectronic devices. Some attempts in this direction have successfully used low-energy nitrogen species supplied by cold plasma or atomic nitrogen beams [25-27]. In this context, the increasing interest in the use of high-quality 2D materials for specialized applications, and the need to modify and leverage the properties of these materials and study their basic properties are indeed one of the most active areas in Materials Physics today.

1.2
Physical properties of TMDs

1.2.1
Crystal and Electronic structure of TMDs

TMDs, in general, have the generic chemical formula "MX_2," where M is the transition metal element, and X is the chalcogen atom. M is a transition metal atom, from the periodic groups' IV, V, or VI, sandwiched in between two layers of chalcogen atoms, as illustrated in Figure 1.1 [28]. Ionic–covalent bonds ensure the stability MX_2 layers, whereas Van der Waals interactions are responsible for keeping the layers weakly bonded, forming a 3D crystal structure. MoS_2 is the most common TMD; it has a hexagonal (H) or rhomboidal (R) symmetry, with trigonal prismatic coordination of the Mo atoms, which are bonded to six S atoms, as seen in Figure 1.1 [29]. Natural Molybdenite occurs in nature mainly as 2H-MoS_2, with two S–Mo–S units per unit cell, whereas the 3R-MoS_2 has three S–Mo–S units per unit cell. This structure is the same found in other TMDs, such as $MoSe_2$, WS_2, and WSe_2. [30]

The electronic properties of TMDs can also be grouped in few classes, having very similar features: MoX_2, WX_2, and most of the compounds where the transition metal is Hf, Zr, Re, Pd, and Pt are semiconducting, whereas NbX_2, TaX_2, VX_2, and other TMDs are metallic. In this chapter, we summarize the semiconducting TMDs having 2H polytype, which becomes 1H in the case of monolayered TMDs, having just one X–M–X sandwich per unit cell [31].

By changing the number of layers of these compounds, one can significantly change or modify the electronic structure of these materials. This

behavior is similar for many different TMDs, such as WSe_2, $MoSe_2$, MoS_2, and WS_2. Generally, the bulk phase of semiconducting TMDs has an indirect bandgap, which transitions to direct bandgap when one isolates a single-layer [32-35].

1.2.2
Vibrational properties

Raman and infrared spectroscopy are powerful and widely used techniques for the structural characterization of solids and molecules. Raman scattering and infrared absorption are strictly related to the vibrational properties of materials, which can be predicted by first-principles calculations [32].

The crystal structure 2H-WS_2 belongs to the point group symmetry D_{6h}. There are 18 vibrational modes at the center of the Brillouin zone, $\Gamma = A_{1g} + 2A_{2u} + B_{1u} + 2B_{2g} + E_{1g} + 2E_{1u} + E_{2u} + 2E_{2g}$. The atomic displacement of the four Raman active modes are shown in figure 1.2. These modes can be readily excited using visible wavelengths. The Brillouin zone is defined as the primitive cell in reciprocal space. Points in the reciprocal lattice set the boundaries of this cell. The Brillouin zone stems from the Bloch wave description (described further in the text) of waves in a periodic medium. It was found that the solutions can be completely characterized by their behavior in the first Brillouin zone.

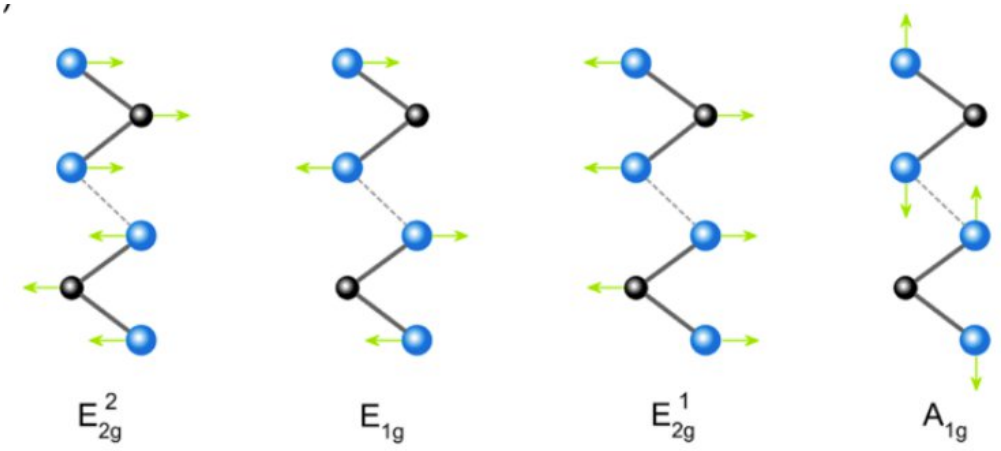

Figure 1.2. Main Raman modes of TMDs. [91]

Monolayer WS_2, also named 1H-WS_2 and having D_{3h} point group symmetry, has nine vibrational modes and six irreducible representations, two translational acoustic, one infrared, and three Raman modes. The rigid shear mode is absent in monolayers [33-35].

The vibrational modes of the monolayer and bulk WS_2 are related, except for the vibrational modes with atomic displacements involving adjacent layers. An

interesting comparison of the phonon modes of bulk and monolayer WS_2 is also possible through their phonon dispersions plotted in Figure 1.3. Both show three acoustic modes, longitudinal acoustic (LA), transverse acoustic (TA), and out-of-plane acoustic (ZA) mode. In bulk WS_2, low-frequency optical modes (E^2_{2g} and B_{2g}) are present, and the modes corresponding to shear and vertical motion of the layers, which are missing in the phonon dispersion of monolayer WS_2 are also present. The E_{2g} and E_{1u} bulk modes collapse into the mode "E'" in the single-layer WS_2. This phenomenon is also evident from the atomic displacements in Figure 1.3: approaching to the monolayer, the displacements of the atoms in the two (independent) layers are equivalent in the E_{2g} and E_{1u} modes [36-39].

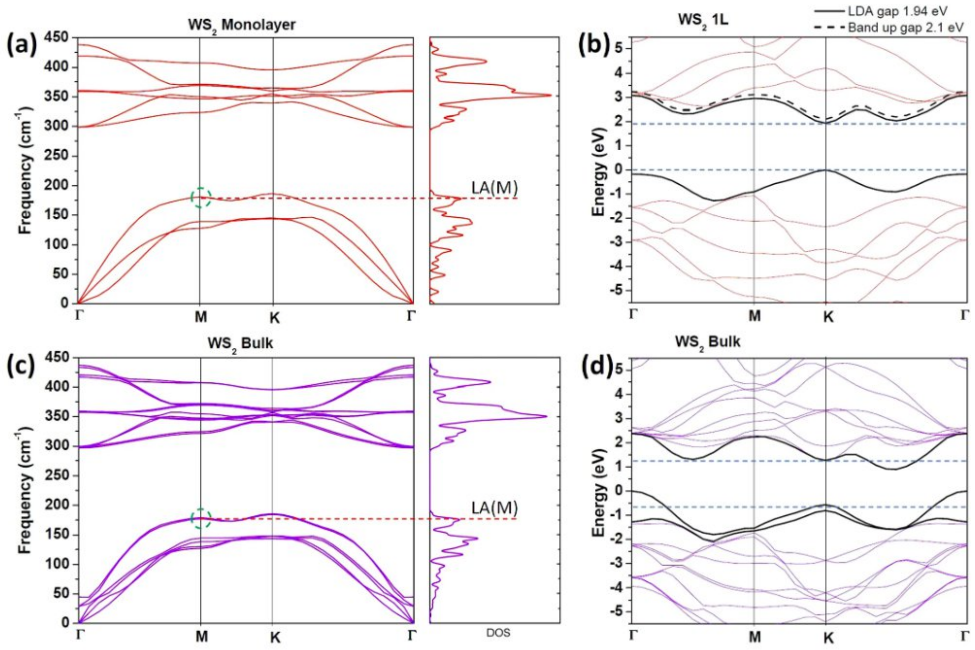

Figure 1.3. (a, c) Phonon dispersion plus density of states [left]; and electronic band structures [right] for WS_2 monolayer [top] and bulk [bottom] (b, d), respectively. [91]

One can observe an increase in frequency for the E_{2g} Raman mode in bulk to the monolayer. Contrary to that, the out-of-plane A_{1g}, being the other main Raman feature, is at a lower frequency in the monolayer WS_2. These shifts in the position of the Raman peaks have been measured experimentally [40] and are used to identify the layer thickness through the Raman spectrum [41]. The plot of the frequency of the E_{2g} and A_{1g} Raman peaks concerning the number of layers highlights a trend in the frequency of the two Raman peaks. The A_{1g} mode increases in frequency with an increasing number of layers, whereas the E_{2g} mode decreases.

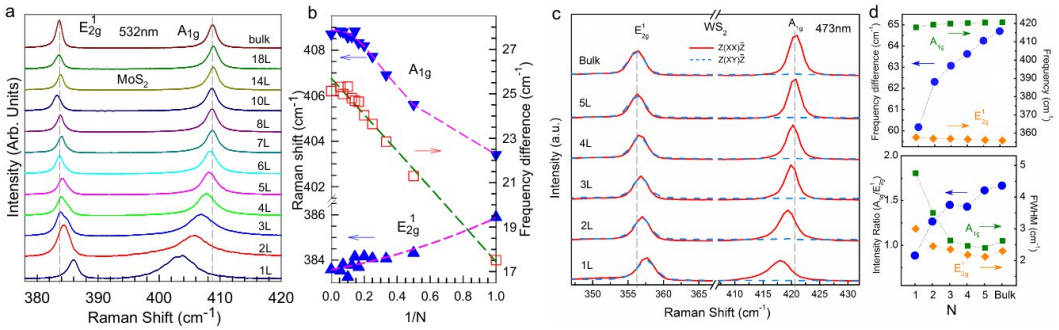

Figure 1.4. (a) Raman spectra of few-layered and bulk MoS_2. The dashed lines indicate E^1_{2g} and A_{1g} positions.(b) Frequency (ω) and its discrepancy (Δω) between E^1_{2g} and A_{1g} phonons as a function of 1/N. (c) Raman spectra of 1-5L and bulk WS_2 with their frequency, frequency discrepancy, $I(A_{1g})/I(E^1_{2g})$ and peak width summarized in (d) [41].

This behavior is widely used in the preliminary analysis of the samples; however, strain effects also affect these peaks and may hinder and mask results in continuous TMD films [42]. The origin of the decrease in the frequency of the E_{2g} with an increase of the number of layers has been identified in the enhancement of the dielectric screening of the long-range Coulomb interactions that overcompensates for the interlayer interactions, resulting in a reduction of the overall restoring force on the atoms [43].

2
Proposals of this thesis

2.1
Motivation

2.1.1
New reliable forms of 2D materials characterization

Today, there are several methods to characterize TMDs, which are widely used in the literature [44-46]. One of the essential methods is employing photoluminescence mapping and fluorescence (FL) microscopy [45]. Both methods rely on the emission of light to identify TMD monolayers. Indeed, either PL maps and low-magnification fluorescence micrographs readily discriminate monolayer structures and films from bulk regions [47, 48]. However, there is a problem when these structures are modified and effectively lose this property, rendering such methods useless [49]. Also, this becomes an issue when the luminescence response is not uniform in the monolayer structure, as is in the case of the WS_2, where usually the PL signal decreases substantially from the edge to the center of the monolayer structures [50, 51].

To correctly identify monolayer structures without relying on only PL maps or FL micrographs, Raman spectroscopy/mapping is another staple option to identify the number of stacked TMD layers [40]. This method is widely used to identify the number of layers by measuring the shift of the main Raman features in the spectra. However, it is also known that this effect may also be present on samples that are under intense mechanical strain [41, 42] or have a large density of defects [49]. In that sense, one may not distinguish monolayers from few-layered structures, only my relying on typical Raman spectroscopy, as the main observed effect may be due to a combination of several factors. Also, low-wavenumber high-resolution Raman spectroscopy may efficiently be used.

Atomic force microscopy (AFM) and optical microscopy (OM) may be used to, in a way, directly identify and discriminate monolayered regions [51]. In the same manner, these techniques also have advantages and disadvantages. In the case of AFM, one cannot probe many triangles at once, and the setup should be

mechanically stable to measure the sample's height correctly. In optical microscopy, the method is only reliable on a few substrates due to the thin-film interference. In this case, the need for a new method, independent of surface modification, substrate, and other parameters are important to characterize monolayers efficiently.

2.1.2
Defect engineering and modification of 2D materials

All TMDs (or all materials in general) have intrinsic defects. This is independent of the synthesis process. Also, this is true and may be represented by the development of the semiconductor industry for the past sixty years [52,53]. The density of defects in TMDs plays a role and can fundamentally change the materials' properties. Indeed, chemically exfoliated WS_2 and MoS_2 monolayers have a higher density of defects, and their electronic properties are considerably inferior to that of CVD synthesized TMD monolayers [100]. However, low density of defects may also improve such properties up to a certain point, as shown in [19,21].

In this way, large scale surface treatments appear as an efficient method to modify 2D materials in general [54]. It generates a low level of surface contaminants like chemicals and is compatible with the production chain of current nanofabrication technologies. In that sense, the research on how defects modify, enhance a given property of 2D materials is fundamental in the subsequent use of them in the semiconductor industry. This means that low-cost and efficient methods that can be applied to many structures are essential, given that the modifications induced by the process are reproducible.

Finally, these defects should be categorized in the dimensionality of defects, the structural effects, and changes in the physical-chemical properties of the materials due to treatment [55]. This categorization is important to understand what is being changed in the structure of the materials and correctly infer what is fundamentally being modified to understand the response of the materials due to a given treatment method [56].

2.2
Project goals

Given these two topics of interest, this thesis was divided such that all the present work converges towards two objectives:

1 New characterization method for fast identification of WS_2 monolayers through Raman spectroscopy.

2 Low-cost, reliable, and fast modification of TMD structures utilizing fast, cold plasma treatment.

3
Straightforward identification method of monolayer WS_2 structures by Raman spectroscopy

3.1
Introduction

In this chapter, we detail a straightforward Raman peak identification method to discriminate monolayer WS_2 crystals from few-layered and bulk samples. Here, this approach is applied to samples prepared by CVD, but it is not restricted to samples prepared by other methods. We show that through the comparison and analysis of other techniques that the strong splitting in A_{1g} mode in close-to-resonance excitation energy condition is a much more convenient identification method than either low-wavenumber Raman spectroscopy, atomic force microscopy, and photoluminescence spectroscopy. We have observed, using a laser excitation wavelength of 647 nm, a characteristic band splitting of ~ 5 cm^{-1} and an increase in the intensity of the red-shifted A^*_{1g} mode, both of which are reliable for layer number characterization.

3.2
Methods

3.2.1
WS_2 synthesis

WS_2 crystal synthesis was carried out using an atmospheric pressure CVD (APCVD) system installed at the Van de Graff Laboratory of the Physics Department/PUC-Rio. The SiO_2/Si wafer was diagonally placed inside an alumina crucible so that 8 mg of WO_3 powder rest under the target substrate. The crucible was inserted in a quartz tube, 25 mm in diameter, inside a single-stage horizontal tubular furnace. Another alumina crucible that housed 300 mg of powdered sulfur was positioned inside the tube upstream out of the furnace. A resistance wire was wrapped around the tube as a heating belt to heat the sulfur powder to 250 °C.

In contrast, the other crucible was centered inside the furnace. A bench-top power supply was used to control the temperature of the heating belt. The

temperature was controlled by setting the electrical current of the power supply, maintaining the temperature at the desired value ; the current was set around 2.0A and 3.0A and the target temperature was controlled visually through a thermocouple.

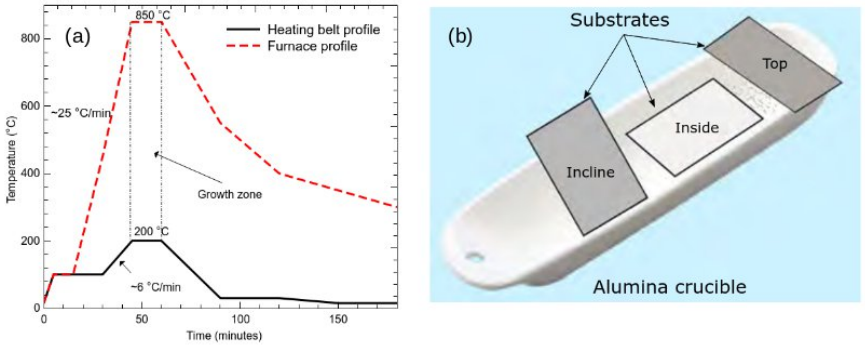

Figure 3.1. (a) Temperature profile for the main furnace and heating belt. (b) Diagonal placement of the substrate inside the alumina crucible.

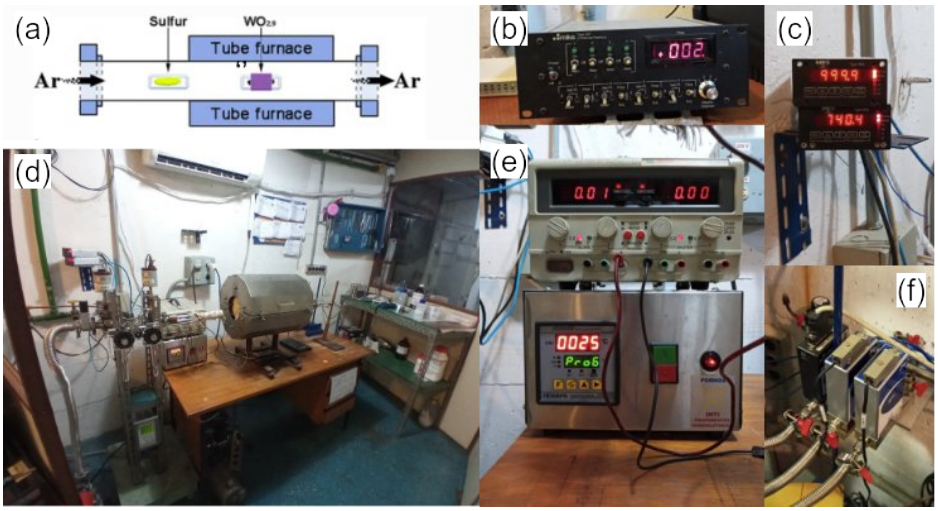

Figure 3.2. (a) A typical APCVD setup scheme for TMD growth. (b) Mass flow controller power supply and readout. (c) Low-pressure readouts. (d) One of the CVD tubular furnaces used in this work can see the pressure gauges and heating belt setup. (e) Furnace and heating belt power supplies. (f) Mass flow controller mount and pure nitrogen bleed valve.

Ultra-dry N_2 was flushed into the system for 5 minutes, followed by a continuous flux of 100 sccm (standard cubic centimeter per minute) of Ar (99,99% pure) throughout the entire growth process to maintain an inert atmosphere inside the reactor. The temperature of the furnace was monitored and maintained at 850°C during the growth. The whole growth process took three hours, from heating

to 850°C and cooling the system back to ambient temperature naturally under a 100 sccm Ar flux. The cooling process is undergone with the furnace closed and the temperature decreases slowly down to ~300°C naturally. This is an important step for the successful growth of WS_2 structures; if the cooling time is shorter, the WS_2 structures will seemingly implode and form irregular structures.

3.2.2

Raman spectroscopy

The Raman effect is the inelastic scattering of light by matter. This effect occurs when light interacts with gas molecules or a solid, leading essentially to its deformation and subsequent vibration (phonons) [57]. Classically, we can derive this effect by studying a molecule polarization vector, that is

$$\vec{P}(r,t) = \alpha \cdot \vec{E}(r,t) \qquad (3.1)$$

Where α is the polarizability of the molecule. In general, molecules do not respond the same way to an electrical field. The polarization vector will behave differently, given the direction of the electrical field. In this sense, the polarizability is a tensor quantity [58]. Hence, one may write equation (3.1) in a tensorial form (mind the summation convention):

$$P_i = \alpha_{ij} E_j \qquad (3.2)$$

Here, P_i represents the components of the polarization vector in the i component, α_{ij} are the components of the polarizability tensor, and E_i are the components of the incident electric field. We can simplify this equation by modeling an isotropic behavior of the Polarization vector; thus, we can simplify the treatment of the effect mathematically without losing insight substance and work with scalar quantities. By taking this into account, equation (3.1) becomes

$$P(r,t) = \alpha \cdot E(r,t) \qquad (3.3)$$

Suppose that a monochromatic light source is used, the electric field may be expressed as a usual plane wave. In this case, P(r, t) is given by

$$P(r,t) = \alpha \Re(E_0 \exp(i\omega t)) = \alpha E_0 \cos(\omega_o t) \qquad (3.4)$$

Given this classical interpretation, we may idealize a diatomic molecule as a mass on a spring [61]. When taking this model into account, the normal

coordinate of the displacement can be expressed as

$$q = q_m \cos(w_m t) \qquad (3.5)$$

By using the small amplitude approximation, the polarizability can be expressed as a Taylor expansion, where the α is a function of the normal coordinate q:

$$\alpha = \alpha_0 + q\partial_q \alpha_{q=0} + \ldots \quad (3.6)$$

Finally, combining (3.6) into (3.4), and using the product to sum transformation rule for cosines, one finds

$$P = \alpha_0 E_0 \cos(\omega_0 t) + q_m E_0 (\partial_q \alpha_{q=0})(\cos(\omega_0 - \omega_m)t + \cos(\omega_0 + \omega_m)t) \quad (3.7)$$

Equation (3.7) shows that; indeed, we have two outcoming electrical fields. The observed increase in frequency is the Anti-Stokes shift, and the decrease in frequency is known as a Stokes shift. The measurement in the change in frequency from the incident light is the Raman effect, which is a means of directly measuring the vibrational frequency of a molecular bond. The first term of equation (3.7) represents the elastic scattering (Rayleigh scattering) [57].

As shown in Figure 3.3, one can see that this results from the incident photon exciting the molecule into a virtual energy state.

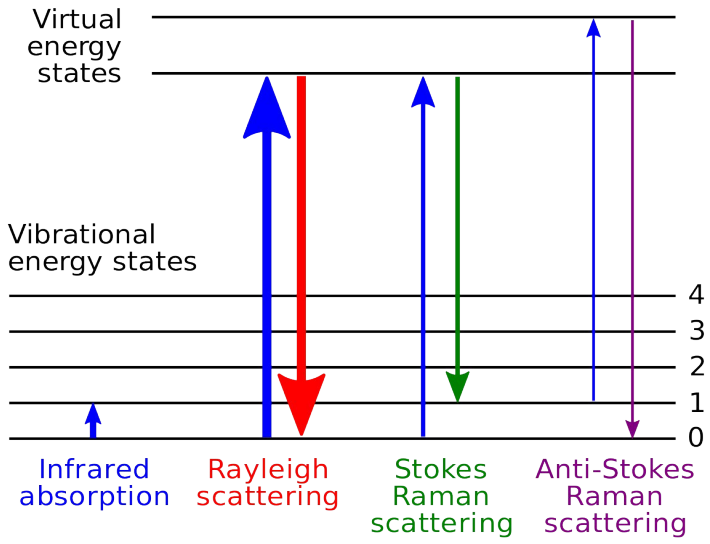

Figure 3.3. Quantum transition diagram for Rayleigh and Raman scattering [58].

Given the interaction, there are three phenomenological possibilities. The elastic process is the first one; the molecule in the excited state can relax back to the ground state and emit a photon of equal energy to that of the exciting radiation. The second case is that the molecule can relax to a real vibrational state and emit a photon with less energy than the incident photon; this is called the Stokes Raman effect or scattering.

Lastly, the other possible outcome is that the molecule is in an excited vibrational state before scattering, which is then excited to a higher virtual state, subsequently relaxing to the ground state, emitting a photon with more energy than the incident photon. This last process is known as the Anti-Stokes Raman effect or scattering. As most molecules will be found in the ground state in ambient conditions, the probability that a photon will be Anti-Stokes scattered is much lower. This is important and loosely explains why Raman measurements are usually done only in the Stokes shift regime in favor of Anti-Stokes.

Although this model is a brief and simple classical description of the Raman effect, there are some inconsistencies with the experiment. Indeed, this model explains how the Raman effect may be used to describe the vibrational modes of molecules in general with relative success. These molecular vibrational modes translate into phonons in the lattice and deserve a more elaborate explanation [57]. Indeed, the quantum nature of these oscillations, even for molecular bonds, will even affect the population (and intensity) of the observed Raman peaks, rendering Stokes shifts more intense. The proper treatment of this phenomenon relies on the time-dependent formulation of quantum scattering [59]. However, we can use the quantum particle interpretation to get some intuition and more insight. The Raman effect can be described as an inelastic scattering of a photon because of the creation or annihilation of a phonon.

The presented classic description does not tell us anything about the intensity of the Raman lines, as it ignores the quantum mechanics behavior of phonons and the population distribution, which relies on the bosonic nature of the phonon field in the crystal. The intensity of the lines of first-order Raman processes relies on the creation and annihilation of harmonic oscillator states describing phonons. In this case, the matrix element for the creation (Stokes) of a phonon is given by

$$I(\omega_0 - \omega_m) \propto |\langle n_k + 1 | q | n_k \rangle|^2 \propto n_k + 1 \qquad (3.8)$$

On the other hand. The annihilation of phonons is related to anti-Stokes lines. Thus, the intensity is proportional to

$$I(\omega_0 + \omega_m) \propto |\langle n_k - 1 | q | n_k \rangle|^2 \propto n_k \qquad (3.9)$$

At thermal equilibrium at a given temperature T, the intensity ration of these two lines is

$$\frac{I(\omega_0+\omega_m)}{I(\omega_0-\omega_m)} \propto \frac{\langle n_k \rangle}{\langle n_k+1 \rangle} = e^{-\frac{\hbar\omega_m}{k_b T}} \qquad (3.10)$$

Where $\langle n_k \rangle$ is described by the Plank distribution. At lower temperatures, the intensity ratio goes to zero, since in this case, thermal phonons are scarce and are not available for annihilation processes [60]. This correctly explains the intensity difference between Stokes and Anti-Stokes peaks.

At some -not so rare- situations, the spectra of materials are collected so that non-trivial phonons are observed. These conditions are possible when one uses an excitation energy higher than the material bandgap and at specific frequencies. This energy regime is called resonant Raman scattering. Under these resonance regimes, extra modes may unravel a wealth of information concerning the vibrational properties of a given material. These extra peaks are related to scattering events involving two or more phonons and other excitation fields inside the material, such as electron-electron, hole-hole, and excitonic scattering events.

In this case, second-order Raman effects, related to the second-order Taylor expansion polarizability coefficients are considered, and the scattering is more complex since the selection rules are relaxed and phonons with several wave vectors are observed (see equation (3.12)), such as higher frequency longitudinal acoustic modes. If there are several atoms in the primitive cell, the intensity distribution of phonons may become difficult to interpret, once many scattering events involving different phonons may occur [61]. A quite simple treatment of the Raman scattering is possible where the frequencies of the excitations are not comparable with the electronic frequencies responsible for the polarizability. For instance, one can consider the pseudo-momentum and energy conservation (frequencies) for scattered phonons as

$$\omega_{exitation} = \omega_{scatt} + \sum_n \pm \omega_n \qquad (3.11a)$$

$$k_{exitation} = k_{scatt} + \sum_n \pm q_n \qquad (3.11b)$$

where the subscripts *scatt* and *n* refer to the scattered and exited phonons, respectively. The plus sign is related to the created phonon excitations, and the minus sign are the annihilated ones. Usually, $||k_{scatt}|| \approx ||k_{exitation}||$ is negligible compared to the dimensions of the Brillouin zone, hence

$$\sum_n \pm q_n \approx 0 \qquad (3.12)$$

This is the typical selection rule for first-order scattering, which restricts the possible phonon excitations around the center of the Brillouin zone. However, this is not true when one considers higher-order contributions. This is particularly intensified, as discussed above, when the excitation energy is remarkably close to optical transition energy, such as an excitonic recombination process. These "resonances" effects influence the Raman scattering process greatly. The Stokes Raman scattering intensity for a given phonon of energy $\hbar\omega_S$ when the excitation energy is resonating with a given state $a\rangle$, that is an eigenstate of the electron-laser and electron-phonon Hamiltonians (so one can expand in terms of $|a\rangle$)**,** is given by

$$I_{phonon}(\omega_S) = \left(\frac{2\pi}{\hbar}\right)\left|\left| \frac{\langle 0|H_{electron-Laser}|a\rangle\langle a|H_{electron-phonon}|a\rangle\langle a|H_{electron-Laser}|0\rangle}{[E_a - \hbar\omega_{Laser} - i\Gamma_a][E_a - \hbar\omega_{Laser} - i\Gamma_a + \hbar\omega_{phonon}]} + C\right|\right|^2 \qquad (3.13)$$

where $H_{electron-Laser}$ and $H_{electron-phonon}$ are electron-laser and electron-phonon interaction Hamiltonians, respectively, and Γ_a is the damping constant for the given resonance [62]. The constant "C" are the contributions of nonresonant scattering. Equation (3.13) combines two scattering processes. In this event, there are two resonances, an incoming and an outgoing, at $\hbar\omega_{Laser} = E_a$ and $\hbar\omega_{Laser} = E_a + \hbar\omega_{phonon}$, respectively. The most pronounced effect is an increase of the Raman scattering signal near these excitation energies. If the intermediate state $|a\rangle$ is a Bloch state [59], the momentum conservation is preserved. The Bloch states are eigenfunctions of the translational symmetry operator of the crystal. These states satisfy the periodicity of the crystal involved. Since the translational operator and Hamiltonian commute with each other, they will have common eigenfunctions. The corresponding eigenvalues are obtained solving the Schrodinger's wave equation using these Bloch wave functions. In this case, the

second-order contributions are not significant enough. However, for a non-Bloch intermediate state, the momentum selection rules are relaxed, hence forbidden off- Brillouin center phonons may be excited with such states [60]. An exciton is not a Bloch state (it is an electron-hole bound state), so these effects are relevant to explain the appearance of these new Raman features at specific frequencies.

In TMDs, the exciton wave functions are tightly localized due to strong Coulomb interaction [62,63], and the relaxation of the momentum conservation becomes pronounced, resulting in several anomalous resonance effects. One can probe the main excitonic transitions through optical absorbance spectroscopy and observe the sharp increase in the reflectance or absorption (depends on the mode of operation) due to the creation of excitonic states [64].

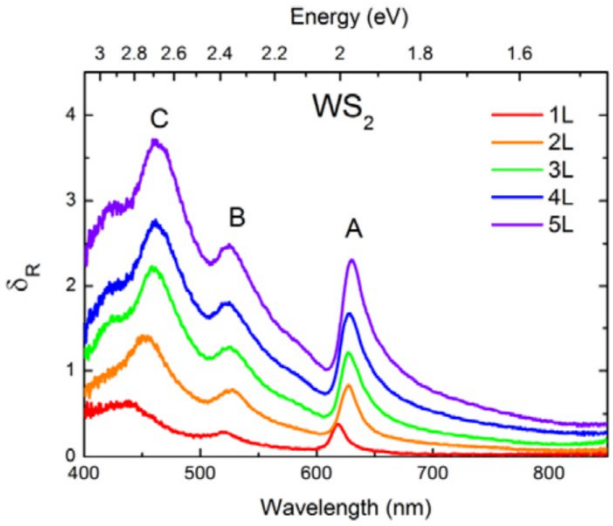

Figure 3.4. Differential reflectance spectra of mechanically exfoliated 2H-WS_2 [64].

Defects also have an important role in the behavior of electrons, holes, and phonons in 2D materials. The double-resonance process involving a two-phonon scattering is also an event which involves an elastic scattering of the excited electron states by localized defects in the crystal structure, and an inelastic scattering event involving the creation of a phonon. The study of defects in TMDs through Raman spectroscopy is still in its infancy. However, one can borrow the expertise in graphene to have a picture of its importance in the characterization of such structures in the probed material: although there are several differences regarding the band structure of graphene to 2D TMDs, the example illustrates the effect of defects and its usefulness [65].

The D band in graphene involves the scattering of an electron by a transverse optical (TO) phonon, in the proximity of the K and K_0 points, and by a defect. This band appears half-frequency of the two-phonon 2TO band (also known as the 2D phonon) frequency and presents a linear dispersion with respect to the excitation energy [66]. The ability to study the defect-related bands in graphene allows one to characterize defect-induced peaks in TMDs. Irradiating MoS_2 sample using Mn^+ ions, one was able to study the density of defects of the materials utilizing Raman spectroscopy. The authors observed the appearance of the LA peak around 227 cm^{-1} and that the intensity ratio of the A_{1g} and E_{2g} modes by the LA peak are proportional to $1/L_D^2$, where L_D is the mean defect distance [67].

It is important to note that not all phonons scatter light. These Raman active modes are determined by selection rules derived in group-theory calculations, provided we know the symmetries related to a given material, space group, and, subsequently, its character table. It is shown that a first-order Raman transition may occur if and only the irreducible representation is the same as one of the irreducible representations which occur in the reduced representation of the polarizability tensor [68].

Moreover, the scattering intensity depends on the geometry of the experiment itself, mainly, the direction of illumination and observation relative to the principal axes of a crystal. The polarization of light and the amplitude of the scattering signal gives information about the symmetry aspects and the lattice vibration responsible for the transition, further helping in the identification and labeling of the observed signals [69].

A good example of this geometric dependence is that the only changing components of the polarizability tensor are the *xy* and *yz* (tensor components) for a given lattice vibration. To observe the Raman effect of that phonon, the polarization of the incoming excitation laser beam parallel to the x-axis and observe the scattered light with its polarization in the y-direction. The analysis of the amplitude of the scattered signal as a function of the polarization, one may determine the Raman active phonons for a given crystalline symmetry [69].

In all used equipment used in this thesis, the backscattering geometry was used so that only specific phonons that are compatible in this geometry are visible. This behavior is also particularly relaxed for more intricate phonon processes when

the two phonons participating in a second-order process belongs to different combinations, as it will be used later, when different phonons with wavevector directed to the M point in the Brillouin zone may interact with one another yielding a characteristic peak in Resonance Raman spectroscopy.

PL, and AFM measurements were performed using an integrated atomic force microscope and micro-Raman spectrometer (NT-MDT, NTEGRA SPECTRA) equipped with a CCD detector and a solid-state laser, which produced an excitation wavelength of 473 nm in backscattering geometry, whose scheme is shown in the Figure 3.5. The spectral resolution is 1 cm^{-1} for Raman measurements and 0.3 nm for PL, using 1800 lines/mm and 150 lines/mm diffraction gratings.

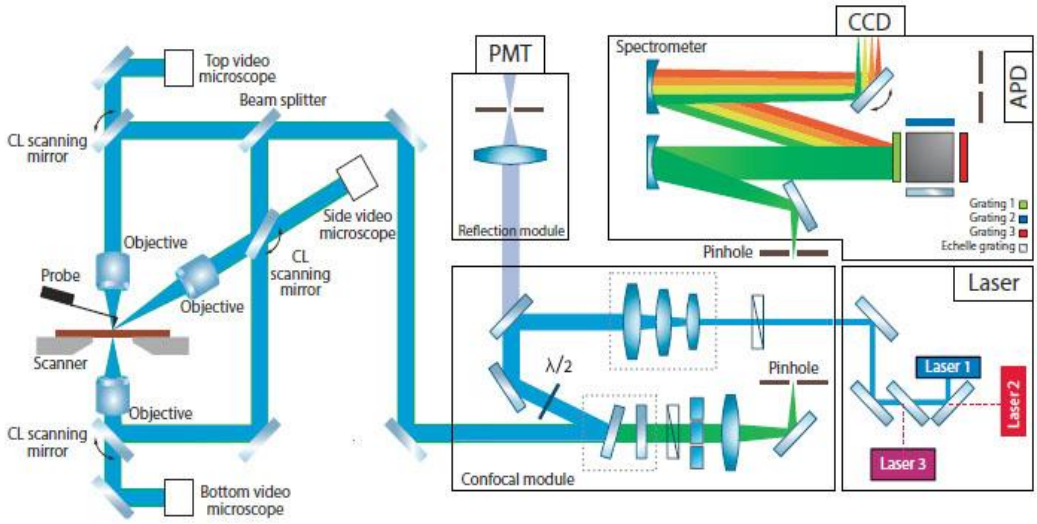

Figure 3.5. NT-MDT NTEGRA SPECTRA Scheme at Physics Department/PUC-Rio. The system used the retro-scattering mount.

High-resolution Raman measurements were performed using the triple stage Raman spectrometer T-64000 of Horiba-Jobin Yvon equipped with holographic gratings (1800 lines/mm) and set in double subtractive/single configuration, and exploiting the excitation of a multiline mixed gas Ar/Kr ion laser (Spectra-Physics, mod. 2018-RM), which allows for an accurate study of very low-energy excitations of low dimensional systems under different excitation energies.

The Raman characterization of low-wavenumber phonons provides a reliable spectroscopic approach that may be used to differentiate monolayer TMDs from multilayer or bulk structures, since it is possible to observe interlayer-

dependent shear and breathing Raman modes. Special care was taken to avoid laser induced-heating and subsequent sample damage. In this-way, different laser powers were used to check any band dispersion effect caused by the laser irradiation. Also, optical density filters were used so the incident power could be controlled to avoid that the laser damaged the samples. Measurements were performed using a 100X objective, giving a laser spot of the order of 1 μm^2 with an incident power of less than 0.2 mW, corresponding to $2x10^4$ Wcm^{-2}.

The used configuration (double subtraction mode) rejects stray light very efficiently. This configuration may be used to obtain spectra of low-frequency bands near to the laser line, depending on the calibration and need, over a broad spectral range. This mode was used alongside 647nm, 514.5nm, and 488nm laser lines to obtain low wave number shear and breathing modes.

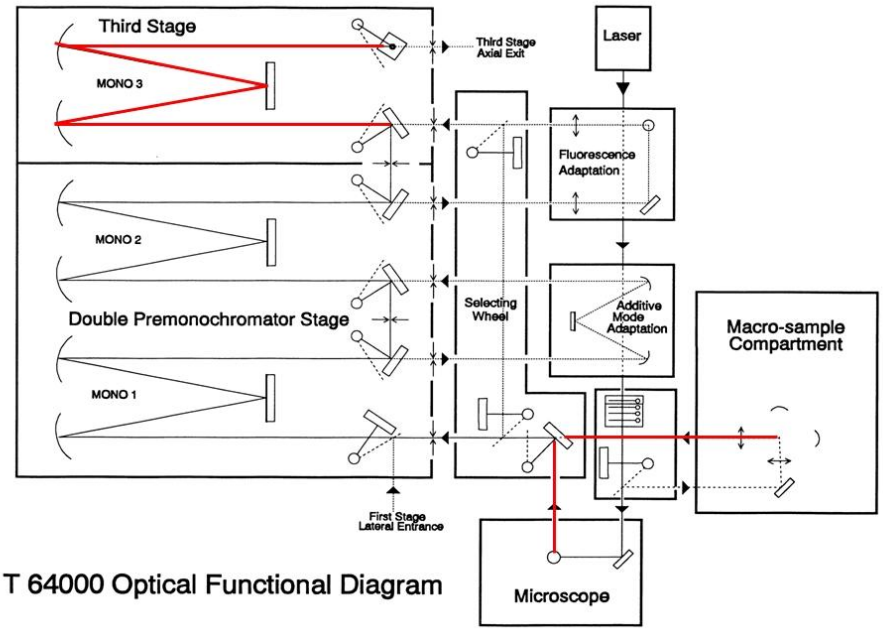

Figure 3.6. Horiba T64000 optical circuit scheme.

Figure 3.7. Horiba T64000 at Verona University and the Spectra-Physics 2018.RM Ar/Kr Laser.

3.2.3

Photoluminescence

When a given direct gap semiconductor is excited by a light whose energy is higher than that of the band bag of the material, it will emit light as a response to such excitation. The same may happen to indirect semiconductors; however, the probability amplitude of such transitions is much lower because this situation involves a third particle, a phonon, needed to momentum conservation. This is the case of the weak emission observed in indirect gap semiconductors such as Si [53].

This is well explained when one excites a material with light close to the bandgap energy, where one may describe the processes through harmonic potential perturbation theory [59]. Photons with energies higher than that of the electronic bandgap are heavily absorbed, generating electron-hole pairs (excitons). Based on this process, semiconductors are the active material in electromagnetic radiation detectors [53]. The inverse process, where the excitons are annihilated, and photons are emitted, also contributes to the luminescence process.

Defects and impurities also play a role, giving rise to the presence of discrete energy levels within the bandgap. In a typical semiconductor, the impurity level is quite low; however, the effects are noticeable and important. This is since the wave function of an electron bound to an impurity or defect level has an interatomic position Δx comparable to the interatomic spacing *a*. Thus, the position uncertainty is responsible for the wavevector uncertainty of the order ~ 1/2*a*. This implies that the transitions involving impurity levels can occur without the participation of phonons; this makes such transitions much more probable than interband transitions. That is why, given the density of impurities and defects, one may improve the luminescence response [53, 60].

Some TMD monolayers are of interest due to its strong photoemission, which makes them good prospects for future applications in many different areas, such as telecommunications, in the case of infrared emission [70]. Although pristine TMDs such as WS_2 and MoS_2 are good light emitters, the proper implementation of defects in their structure may significantly improve their PL, such as vacancies, dislocations, as well as other structural defects [31, 71]. Hence the interest in the modification of such monolayer structures.

PL measurements were performed using the integrated AFM and micro-Raman spectrometer (NT-MDT, NTEGRA SPECTRA) equipped with a CCD detector and a solid-state laser, which produced an excitation wavelength of 473 nm in backscattering geometry. The spectral resolution is 0.3 nm for PL, using a diffraction grating of 150 lines/mm.

3.2.4

Atomic force microscopy

The topography of WS_2 structures was investigated employing the equipment described in section 3.2.3: NT-MDT NTEGRA. AFM images were taken in contact mode using a Si tip. Topographic images were processed with a first-order plane filter to eliminate the tilt between the sample and the microscope. The AFM measurements were made at room temperature and humidity of around 40%.

When the sample is mounted into the AFM piezoelectric drive, the AFM tip slowly approaches the sample. Once contact is made, detected by the laser deflection in the photodiode, the approach halts. The system is adjusted so that the desired set point (essentially the contact force between the tip and the sample)

was fixed. Then, the sample is scanned in the x and y direction, where the vertical movement of the tip may measure the height variation at each point as well as the torsion of the cantilever, which qualitatively gives the friction force between the tip and the scanned surface [72, 73].

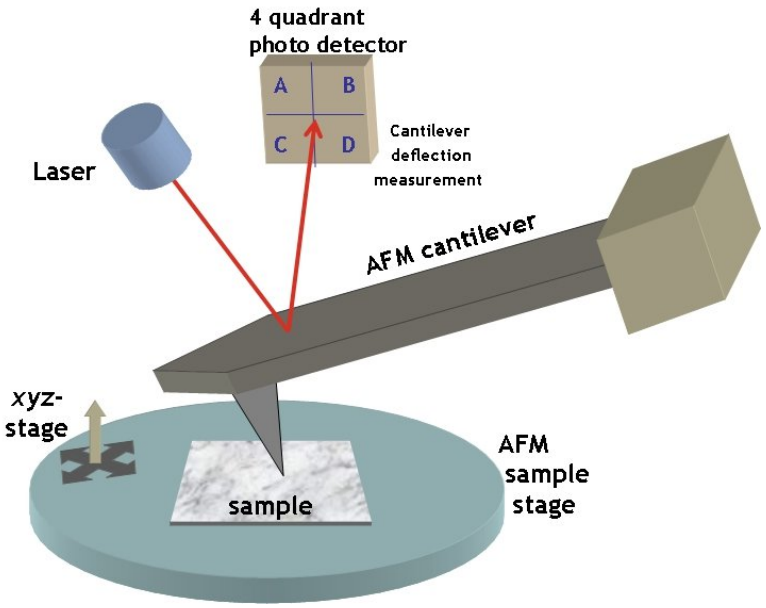

Figure 3.8. Operation scheme of a typical AFM setup. The movement of the piezoelectric stage interacts with the cantilever tip. The topographic features cause an upwards deflection as well as a principal axis deformation of the cantilever. This effect is detected as a change in the position of a laser spot on a photodetector array.

In the operation mode used in this thesis, a feedback loop is implemented so that the vertical force remains constant throughout the measurement. This is the so-called constant force mode. In this particular mode of operation, the output from the feedback will yield the sample surface topography to within a small error, constrained by the roughness of the sample, the tip geometry, and scanning parameters, such as tip velocity, number of points, etc. [74, 75].

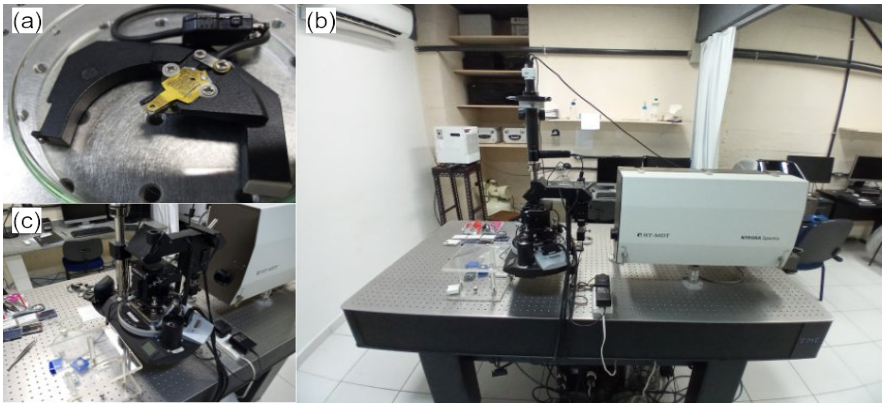

Figure 3.9. (a) AFM tip mount. (b) AFM stage with Coupled Raman/AFM/PL head on top. (c) Side view of the NTEGRA used in this thesis (Van de Graaff Laboratory, Physics Department/PUC-Rio).

3.3
Results and discussion

In Figure 3.10(a), an AFM image of a 10 μm triangular crystal of the WS_2 film is shown. In the image, we can see the color contrast between the substrate and the triangle. The step height was 0.9 ± 0.2 nm, where 0.2 nm is the standard deviation of the measurements (Figure 3.10(b)). Also, to characterize few-layer regions, AFM and PL maps were performed. The height measurement was compatible with the lack of luminescence in the center of the crystal due to the indirect-to-direct bandgap transition that appears when one isolates a single layer of WS_2 (Figure 3.10(f)). The measured step height at the center of the WS_2 is 2.3 ± 0.2 nm, as seen in Figure 3.9(e).

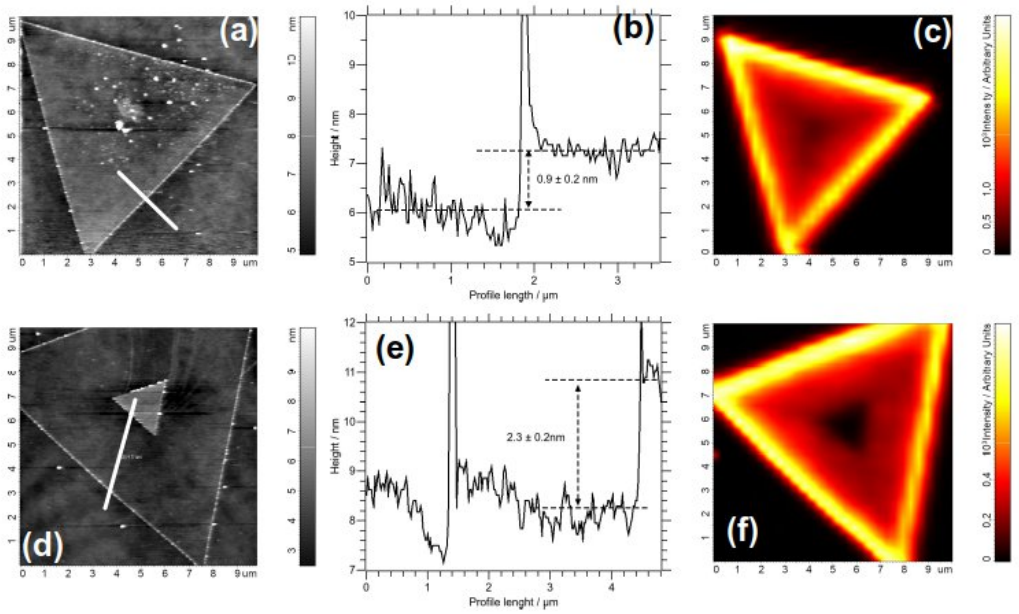

Figure 3.10. AFM topography, profile, and Photoluminescence map of monolayer and trilayer WS_2: a) AFM image of monolayer WS_2. (b) Step height profile showing ~ 0.9 nm difference between substrate and monolayer. (c) Characteristic PL map for monolayer triangles with the typical inwards PL intensity signal loss. (d) Trilayer triangle topography showing the center trilayer structure and (e) Step height profile showing ~ 2 nm height difference from the monolayer base to center triangle structure. (f) PL map of the same triangle highlighting the lack of luminescence in the center of the structure where the trilayer region is present. Unlike monolayer structures, the presence of a second layer abruptly quenches the PL signal due to the direct-to-indirect bandgap transition. White lines in Figure. 3.9(a) and Figure. 3.9(d) are related to profiles in Figure. 3.9 (b) and Figure. 3.9(e), respectively.

In Figure 3.10(f), the measured PL intensity decreases inwards and then vanishes due to the presence of an extra WS_2 triangle stack in the center of the structure. Due to this progressive signal loss behavior, the PL is not conclusive to show whether the structure presents nanoscopic defects, which may affect the signal or have nanometric stackings, which is unlikely. On the other hand, it is known that this PL intensity reduction is typical of such monolayer structures (Figure 3.10 (c)) [46, 76]. However, defects may play a role also due to the change in the overall band structure of the material in the presence of such structural features [77]. One possible explanation is that different edge passivation in WS_2 could induce different spin states in which the magnetic properties at the edges change. In a theoretical work where first-principles calculations indicate that the

high spin density is indeed localized in metallic vacancies at the edge [62]. By taking this into account, likely, one may not distinguish well-oriented bilayer WS_2 from perfect monolayer. This technique, however, is efficient in the case of misaligned or incomplete bilayer regions, since such smaller features would generate irregular and scattered dark spots over the monolayer structure.

Even though the peak positions of the main Raman modes E_{2g} and A_{1g} are frequently used to distinguish WS_2 structures as a function of the number of layers, it is known that their positions are affected by several factors, such as strain and doping [31]. In this case, the determination of the number of layers based on the shift difference of these peaks, as usually done [46], is not reliable because the supporting substrate may influence the determination of these peaks positions.

For most TMDs, low-wavenumber Raman spectroscopy may be used as a reliable means to differentiate monolayer structures from few-layered materials [62]. In that case, it is possible to observe the shear and breathing modes that appear only for layered regions. However, since they red-shift beyond the monochromator cutoff wavenumber (~8 cm^{-1}), these modes are not observable for multilayer structures, as shown in Figure 3.11(a). In general, it is impossible to distinguish from three-layer to other multilayer structures. Here it is possible to observe the progressive redshift of the breathing mode for bilayer and few-layered structures and the vanishing of the low-wavenumber peaks for multilayered structures when the samples are excited with a 488 nm laser. In Figure 3.11(b), however, an additional peak related to the in-plane mode E^2_{2g} is present in the spectrum obtained with a 514.5 nm laser, independent of the number of layers. In that case, it is impossible to distinguish few-layered WS_2 structures. The in-plane mode E^2_{2g} may incorrectly be assigned for multi-layer structures. However, the repeated measurements with other wavelengths rule out this possibility, as this mode is present in near bandgap resonance Raman spectra.

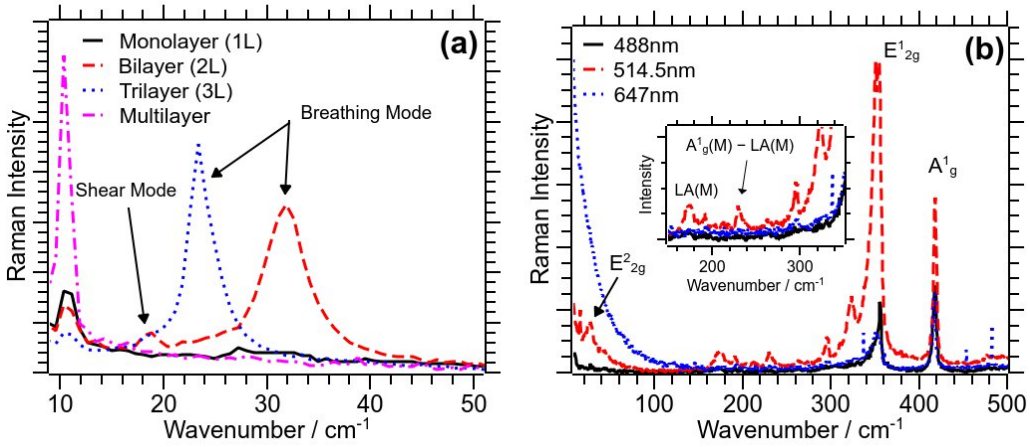

Figure 3.11. (a) Low-wavenumber Raman spectra of WS_2 structures were recorded under excitation at 488 nm. The absence of breathing and shear modes is characteristic of monolayer structures. The breathing mode red-shifts and vanishes for multi-layered structures; in this case, one can distinguish 1L, 2L, 3L, and few-layered structures. (b) The in-plane mode E^2_{2g} peak present with 514.5 nm excitation wavelength and comparison with 488 nm and 647 nm. This peak is only present along other resonant-Raman peaks. The inset in (b) highlights some resonant peaks that are related to collective motio of the atoms in the lattice.

The low-wavenumber peaks related to shear and breathing modes are only present because of interlayer interactions, the peak positions shifting with the number of layers, and as shown in Figure 3.11(a). Moreover, the low-wavenumber region below 150 cm^{-1} is not very accessible in many commercial Raman spectrometers. The characterization and determination of the number of layers through careful low-wavenumber analysis may also be affected by the presence and subsequent excitation of the E^2_{2g} mode, peaked at about 24 cm^{-1}, which appears only when 514.5 nm excitation energy is being used.

Figure 3.12(a) shows the Raman spectrum of single (1L), bi (2L), tri (3L), and multi-layer WS_2 samples measured under a 633 nm excitation line. From this figure, the emergence of the A_{1g} splitting due to the stacking of WS_2 layers is evident. The relative intensity ratio of A_{1g}/A^*_{1g} increases as a function of the number of layers, as observed in Figure 3.12(a). There are not many reports in the literature that highlight this effect in near resonance measurements. In fact, to the best of our knowledge, there are only a very few works that observe this splitting in the out-of-plane A_{1g}-modes in WS_2 and other TMDs, such as references [78, 79].

According to [80], there are some possible reasons for this split. One of those is the in-plane orientation of the A exciton wave function involved in the resonant Raman scattering process. However, such a splitting is also observed in off-resonance measurements. In this case, the chance of an excitonic contribution to such an effect is unlikely.

In this way, one, in principle, may differentiate the number of WS_2 layers by measuring the peak difference and intensity. Performing the Raman measurement with different excitation energies is the key to observing the dependency of this effect with the laser wavelength. Figure 3.12(b) highlights A^*_{1g} dependency as a function of excitation wavelength. It is possible to observe that the new peak is only present when bilayer samples are excited with laser energies close to the band-gap energy.

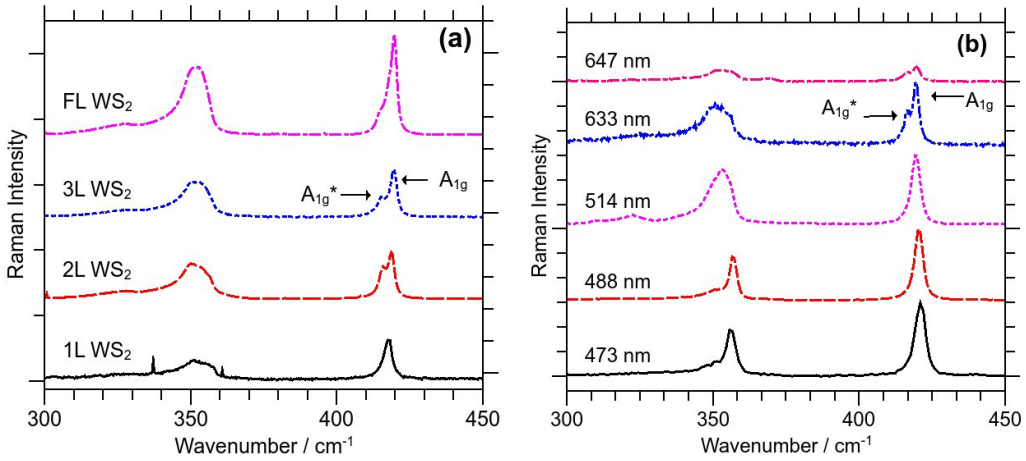

Figure 3.12. (a) A_{1g} vs. A^*_{1g} splitting emergence as a function of layers. The spectra were excited by the 633 nm line, (b) A^*_{1g} dependency as a function of excitation wavelength in bilayer samples. It is possible to observe that the new peak is present when bilayer samples are excited with laser energies close to the band-gap energy (632 nm).

In Figure 3.12(b), the A^*_{1g} shoulder feature was only present when the exfoliated samples were excited at 633 nm. This is evidence that this feature is dependent on the excitation energy. Also shown in Figure 3.13(a), for oriented and inverted to one another. It is clear that such spectral behavior is independent of the orientation of the layers while the resonance effect is clear when we zoom the image around A_{1g} peak position (Figure 3.13(b) for excitation light of 532 nm and 633 nm wavelengths. Optical micrographs are shown in Figure 3.13 (c-e).

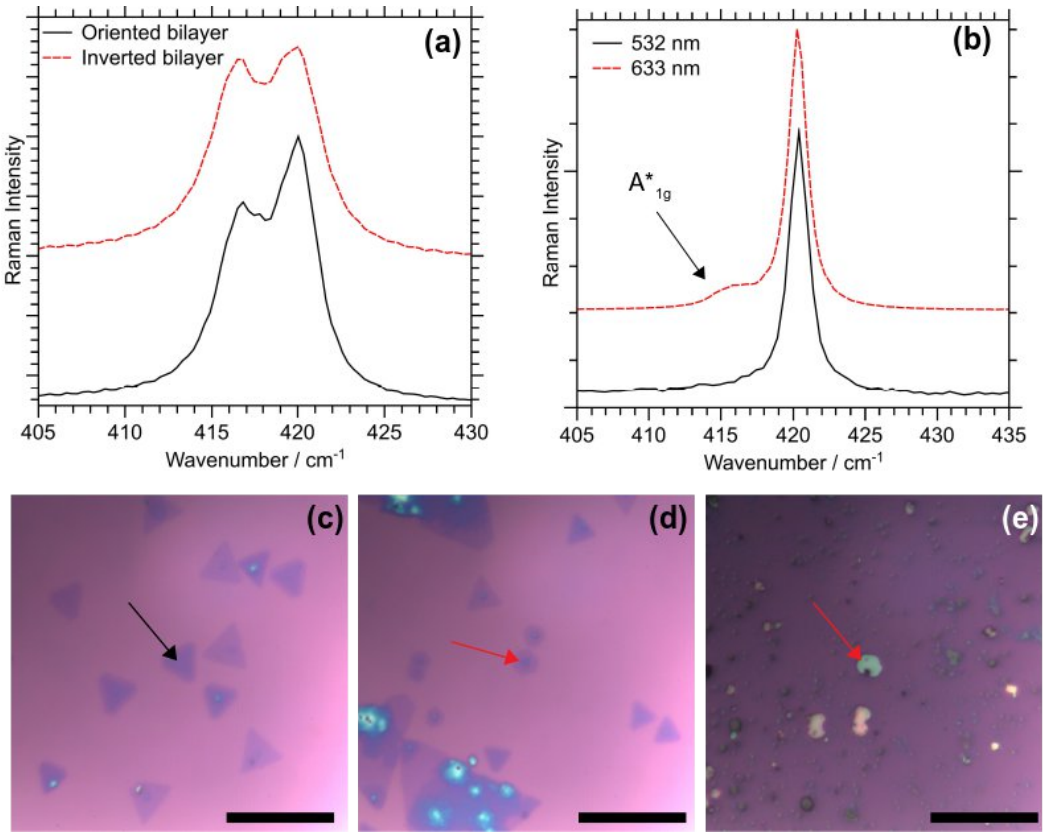

Figure 3.13. (a) Raman spectrum of oriented and inverted bilayer WS_2 samples. (b) A^*_{1g} split emergence in multilayer exfoliated WS_2. The A_{1g} remains symmetrical for 532 nm, and A^*_{1g} is present blue-shifted around 5 cm^{-1} from the main A_{1g} peak. (c-d-e) optical micrographs of oriented bilayer triangle, inverted bilayer, and exfoliated multilayer WS_2., respectively. The blue and white spots in (d-e) are multilayered regions. The scale bar in the figures is 20 μm.

Figure. 3.14(a) shows the Lorentzian peak fitting with the presence of a third peak component in between A_{1g} and A^*_{1g} main peaks, which is strong evidence for few-layer WS_2 structures measured with 633 nm laser. The progressive intensity and the splitting difference may be appreciated in Figure 3.14(b). The splitting value as a function of layers increases from 0 to ~ 5 cm^{-1}, for several different measurements, which is well beyond the wavelength resolution of most spectrometers. This splitting is then an absolute spectral feature for determining the number of layers, further confirmed by AFM and low-wavenumber measurements with 488 nm excitation laser. Indeed, one may also compare the relative A_{1g}/A^*_{1g} intensity ratio; however, such a feature is dependent on the experimental arrangement of the measuring equipment as well.

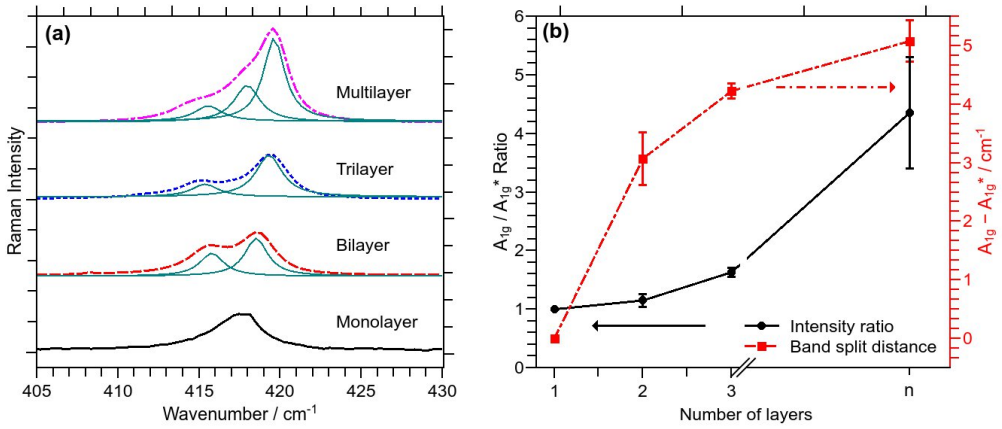

Figure 3.14. (a) The fit of the Raman spectral profiles observed in the region between 410 and 430 cm^{-1} using Lorentzian curves. The splitting distance is evident from 2 to 3 WS_2 layers. For multilayer stacks, there is the appearance of a third peak contribution between A_{1g} and A^*_{1g}. (b) Splitting distance as a function of the number of layers, independently determined by low wavenumber measurements with a 488 nm laser line. The difference between the maxima of the fitting Lorentzian curves is 3.1 cm^{-1} for bilayers, 4.2 cm^{-1} for trilayers, and 5.1cm^{-1} for multilayer stacks, respectively.

One important aspect of the results shown in Figure 3.14 (a) is the increase in the intensity of deconvoluted peaks as a function of the number of layers. This spectral feature becomes prominent when the samples are excited with energies close to the main excitonic transition, which indicates it is a resonant excitation. One cannot, however, assign these peaks to a forbidden phonon. Instead, several reports identify such split for other layered materials [81-83], mainly due to Davydov splitting.

In that sense, what we observe is that the interlayer interaction (or the presence of two or more layers), and attest that, if the probed region has two or more layers, such interaction will always be present, independent of other effects. Indeed, this effect is due to the presence of different atoms in the unit cell, which further decreases the symmetry and lifts the degeneracy related to some quantum numbers, in this case, vibrational quantum numbers [84]. Unlike other resonance Raman peaks, which are amplified either at around 514nm or 633nm excitation wavelengths. This feature is particular to the latter, which rules out the typical multi-phonon interactions present in resonance Raman spectroscopy.

4
Photoluminescence of WS_2 monolayers changes under low-power plasma treatment

4.1
Introduction

In this section, we will report the modification in PL by creating defects via conventional low-power Ar plasma treatment. We found that the PL signal from WS_2 monolayers is gradually shifted and quenched as a function of treatment time. Also, Raman spectra of the treated WS_2 monolayers show that the E_{2g}/A_{1g} peak position difference does not change, which suggests that the treatment is not imposing a mechanical strain due to the creation of vacancies. Only for long exposure treatment, the out-of-plane peak A_{1g} mode suffers a slight intensity decrease. Moreover, X-ray photoelectron spectroscopy (XPS) does not show an increase in W-O related bonds, suggesting that these effects are only due to vacancies in the crystal lattice, a consequence of our Ar plasma treatment. AFM also revealed that the roughness increased, further confirming the damage of the crystal microstructure.

Furthermore, we will describe the change in light emission properties of WS_2 monolayers via straightforward N_2 plasma treatment. The PL signal gradually improved for short treatment times and quenched for longer periods of plasma exposure. Raman spectra of the treated WS_2 monolayers show that the E_{2g}/A_{1g} peak positions did not change significantly, suggesting that the treatment is not imposing a significant sort of mechanical strain or substantial lattice deformation, as in the case of argon plasma treatment.

The Raman peak intensity of the treated WS_2 LA(M) phonons related to the density of defects in the crystal increases. Finally, XPS suggested the presence of N atoms incorporated into the lattice, being responsible for an enhancement of photoemission and p-doping of the material. AFM images suggest that the short treatment times impinge minimal damages to the sample's surfaces.

4.2
Experimental details

4.2.1
Sample preparation and plasma treatment

The synthesis of monolayer WS_2 structures was performed following the experimental details found in the last chapter. After the growth, the samples were placed in the Harrick Plasma PDC-32G-2 plasma cleaner installed at the Physics Department of PUC-Rio. The vacuum chamber was pumped out for 5 minutes and flushed with Ar gas to remove most leftover water and other gas residues. After this purging process, a controlled flow of 15 sccm (standard cubic centimeter per minute) of Ar (or N_2) was inserted in the camber. The gases purity is 99.99% and they are supplied by Messer Gases Brazil. The cold plasma was then generated using an RF coil, and the treatment lasted from 1 to 8 seconds with a power density of 7 W/cm^2. After the plasma treatment, the samples were stored in a vacuum environment to avoid ambient moisture and degradation.

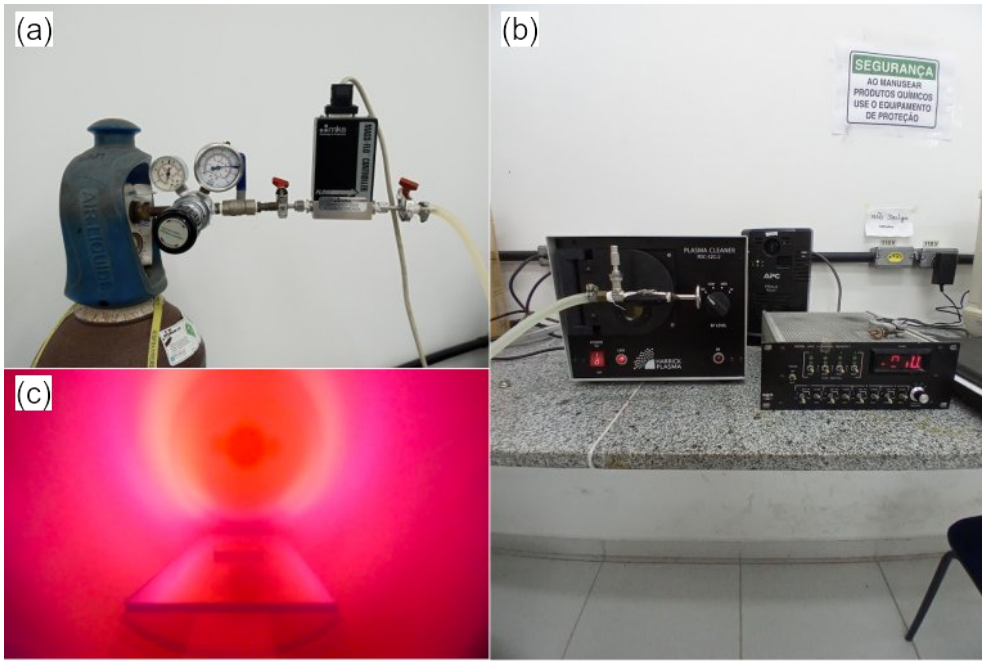

Figure 4.1. (a) Mass flow controller mounted on the desired gas manometer/cylinder. (b) Harrick Plasma PDC-32G-2 setup with mass flow controller (MFC) power supply. (c) Sample undergoing plasma bombardment.

4.2.2

Raman spectroscopy and Photoluminescence

Raman spectroscopy was performed following the same experimental protocol as the last chapter. However, PL maps were performed using the Horiba LabRAM HR Evolution at the department of physics, Penn State University. It is equipped with solid-state, 532nm, laser, and 150 lines/mm grating for a broader spectral range. Measurements were performed using a 100X objective, giving a laser spot of the order of 1 μm^2 with an incident power of less than 0.2 mW, corresponding to $2x10^4$ Wcm^{-2}.

The LabRAM HR Evolution Raman spectrometers are ideally suited for both micro and macro measurements. The Confocal Raman microscope enables the most detailed images and analysis to be obtained. They are widely used for standard Raman analysis, Photoluminescence (PL), Tip Enhanced Raman Spectroscopy (TERS), and other hybrid methods.

Figure 4.2. LabRAM HR evolution was used for Raman and PL measurements.

4.2.3

X-ray photoelectron spectroscopy and Atomic Force Microscopy

X-ray photoelectron spectroscopy is a surface chemistry analysis used in a wide range of materials and purposes. XPS is used for elemental analysis, as well as to study the electronic state of a given material. By irradiating the sample surface with X-rays, one can obtain the characteristic XPS spectra of the probed surface, measuring the kinetic energy of photoelectrons emitted from the topmost layers of the material. A photoelectron spectrum is obtained by counting ejected photoelectrons over a range of kinetic energies [85].

The high energy of the X-Ray photon is enough to ionize the core-level of the majority of atoms. The energies and intensities of the photoelectrons give a specific kinetic energy peak [86]. The identification and quantification of all surface elements are possible using this technique, with the obvious exception of hydrogen [87].

Photoelectronic interactions can only occur when the electron bond energy is lower than the exciting photon energy [86]. Part of the photon's energy is used to remove the electron from the atom, and the other part is transferred to the electron as kinetic energy. An electron analyzer can measure the distribution of photoelectron kinetic energies, and thus a spectrum is obtained. The function of the analyzer is to collect the emitted electrons and measure their kinetic energies. From the conservation of energy principle, one can say that

$$E_f = E_i \rightarrow E_n + \hbar\omega = E_{ex} + E_{electron} \qquad (4.1)$$

Where E_n,E_{ex} are the neutral and the excited energies of a given atom and $E_{electron}$ is the kinetic energy (KE) of the removed electron by the incoming photon of energy $\hbar\omega$, $\hbar$ being the reduced Plank constant and ω the photon angular frequency. It is quite straightforward to rearrange this simple equation so that one can derive the electron energy:

$$[E_n - E_{ex}] + \hbar\omega = E_{electron} \qquad (4.2)$$

The difference term inside the brackets is essentially the electron binding energy (BE). Hence, one may write (4.2) as

$$BE + \hbar\omega = KE \quad (4.3)$$

The above equation is only valid by taking the vacuum as a reference for the zero energy. However, we will be working with solids, and in this case, the Fermi level is used as a reference for the energies. In this way, a correction in equation (4.3) is necessary to include the spectrometer work function, which is also a barrier to electron photoemission. Indeed,

$$BE + \hbar\omega + \varphi_E = KE \qquad (4.4)$$

Where $\varphi_E = E_{vac} - E_{fermi}$ is the work function of the spectrometer and E_{fermi} and E_{vac} are the fermi energy and the vacuum energy, respectively. Since the

sample stage and the chamber are grounded, the work function may be neglected [87].

XPS analysis was performed in a surface analysis chamber installed at the Van de Graaff Laboratory, PUC-Rio, and equipped with a VG Thermo Alpha 110 hemispherical analyzer with seven channeltron detectors and using Mg-K_α line as the x-ray source. The measurements were performed with the analyzer positioned at an angle of 90º with respect to the sample surface normal. Further, the possible surface charge effect (shift in electron energy) was monitored using the C1s (C–C) photoemission line at a binding energy of 284.6 eV. Peak fitting was performed using the CasaXPS code and assuming a Shirley background, which considers the inelastic scattering of the electrons**.** AFM was performed using a Bruker Icon system at the Millennium Science Center at Penn State, configured to work with Peak Force tapping mode.

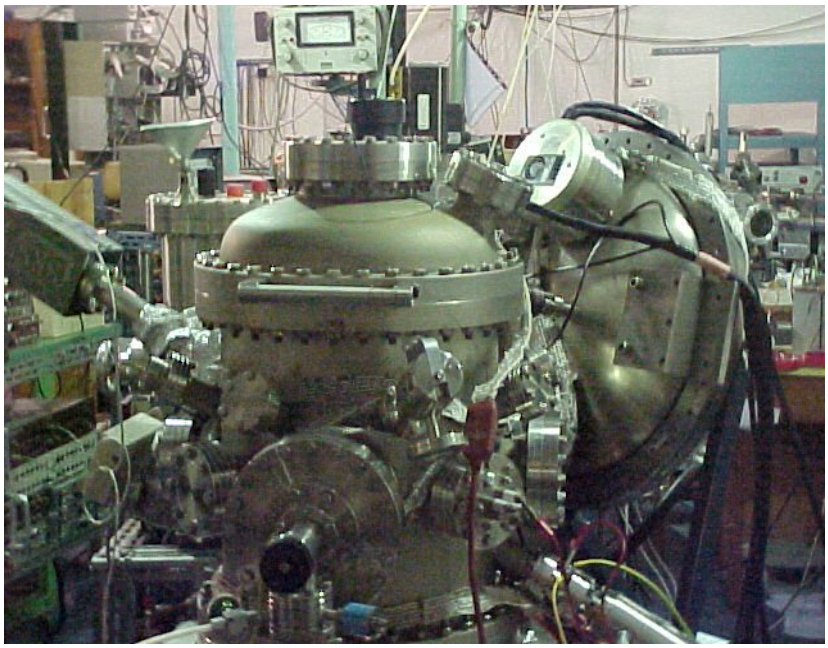

Figure 4.3. XPS Chamber and its support equipment used in this work.

4.3
Ar Plasma results

Figure 4.4 resumes the Raman results obtained from WS_2 monolayer samples using a 514.5 nm laser wavelength. The progressive broadening of the second-order 2LA(M) phonon at around 350 cm^{-1} upon the increase of the treatment time is clear in Figure 4.4(a), which suggests stronger damping constant

due to increasing phonon-phonon scattering and decreasing phonon lifetime [67]. This behavior is expected, as it is an indication of defects in the lattice. This peak resonates with the B exciton direct transition, which is slightly amplified with the higher concentration of point defects in the lattice. However, due to the heavy suppression of electron-hole recombination, we could not observe the B exciton PL for the treated samples. The 2LA(M) phonon is convoluted with the in-plane E_{2g} mode at 355 cm^{-1}, as shown in Figure 4.4(a-b). The only observed change on the A_{1g} mode peak (at around 415 cm^{-1}) is the reduction of its intensity relative to the 2LA(M)+E_{2g} peak.

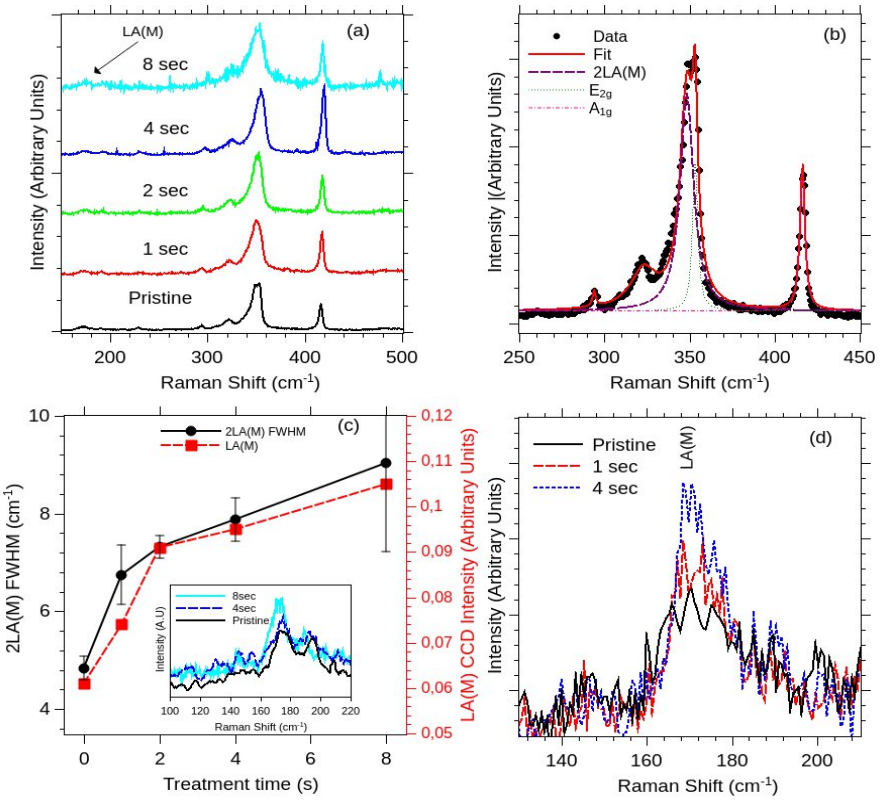

Figure 4.4. (a) Raman spectrum of WS_2 monolayers. It is possible to observe the increasing 2LA(M)+E_{2g} peak broadening due to the plasma treatment (b) Deconvolution of the main WS_2 peaks of the pristine sample, (c) Evolution of the 2LA(M) FWHM as a function of the treatment time (black dots), together with the slight intensity increase of the LA(M) mode, whose spectrum is shown in the inset, as a response to the treatment (red squares). (d) Cross polarized spectra of the samples. The amplitude increase of the LA(M) is visible and indicates a higher defect concentration in the samples. The laser wavelength was 514.5nm.

It is shown in Figure 4.4(c) that the LA(M) peak increases upon the plasma

treatment time. This peak is the LA mode near M point at Brillouin zone, and therefore, it is not a first-order Raman peak. It originated from a double resonance process involving one inelastic phonon scattering and one elastic defect scattering. It can be Raman active only due to the presence of defects in the crystal lattice. Besides, the cross-polarized Raman spectra did not reveal any new defect-related peaks or features other than an intensity increase of the LA(M) peak, as can be seen in Figure 4.4(d), in agreement with previous results [88].

Also, there is no significant spectral change due to the treatment of the samples in few-layered regions that can be selected using the number of layers identification method by Raman developed in [49]. This means that one can differentiate single layer treated samples without relying upon the presence of a strong luminescence response.

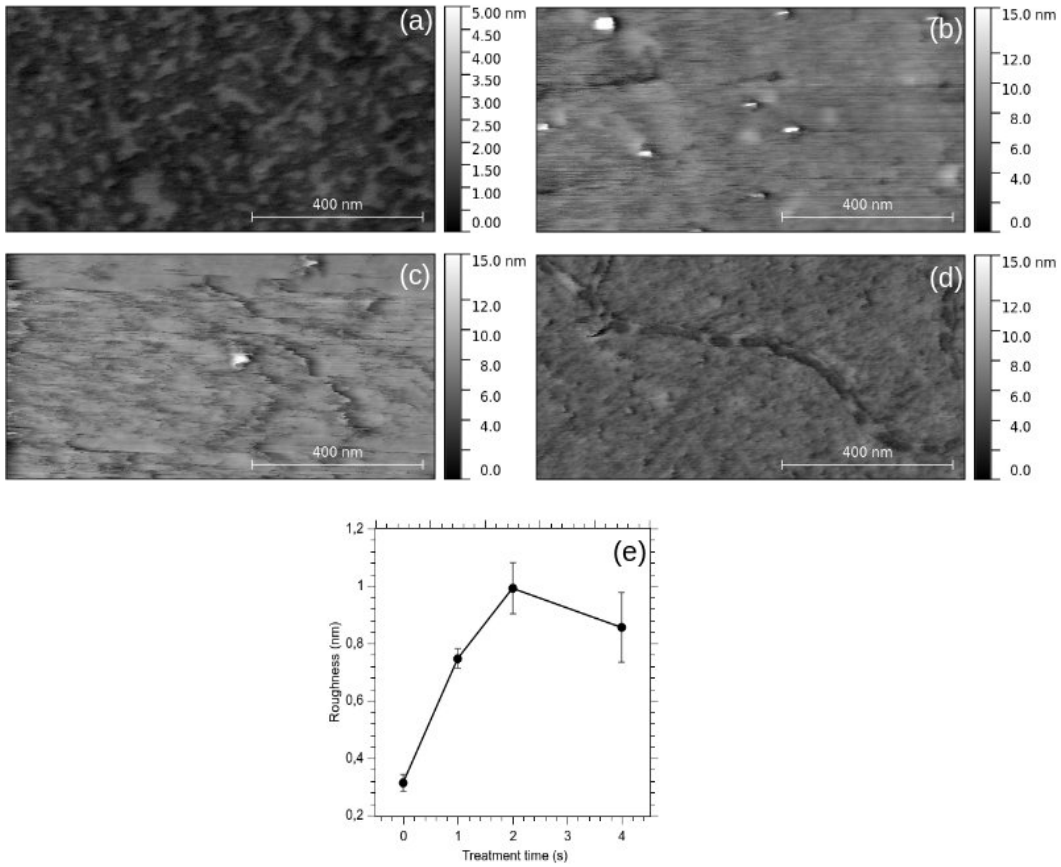

Figure 4.5. (a-d) Atomic force micrographs of pristine and samples treated for 1s, 2s, ad 4s, respectively. Note the difference in the vertical scale between figures 4.5(a) and 4.5(b-d). (e) roughness evolution due to Ar plasma treatment.

These results suggest that the system is losing its crystallinity after long

periods of plasma bombardment, the LA(M) mode, and second-order resonant 2LA(M) phonon show evidence of high defect concentration as a result of the plasma surface treatment. AFM images of pristine and plasma-treated WS_2 flakes are shown in Figure 4.5. The images obtained from treated samples show the presence of cracks and particles that are absent on the pristine sample (Figure 4.5(a)). We can illustrate the evolution of the sample degradation by evaluating the roughness as a function of treatment time, as shown in Figure 4.5(e). The obtained results indicate the progressive increase in the damaging of the samples.

One of the main problems dealing with the PL response of WS_2 crystals is the progressive inward loss of signal intensity of monolayered-structures. This is a challenge since the behavior is due to the higher concentrations of defects inside the triangular-shaped structures [89]. The PL maps of samples subjected to plasma treatment for different times are shown in Figure 4.6. The PL maps were obtained by using laser light with 532 nm wavelength as the excitation beam.

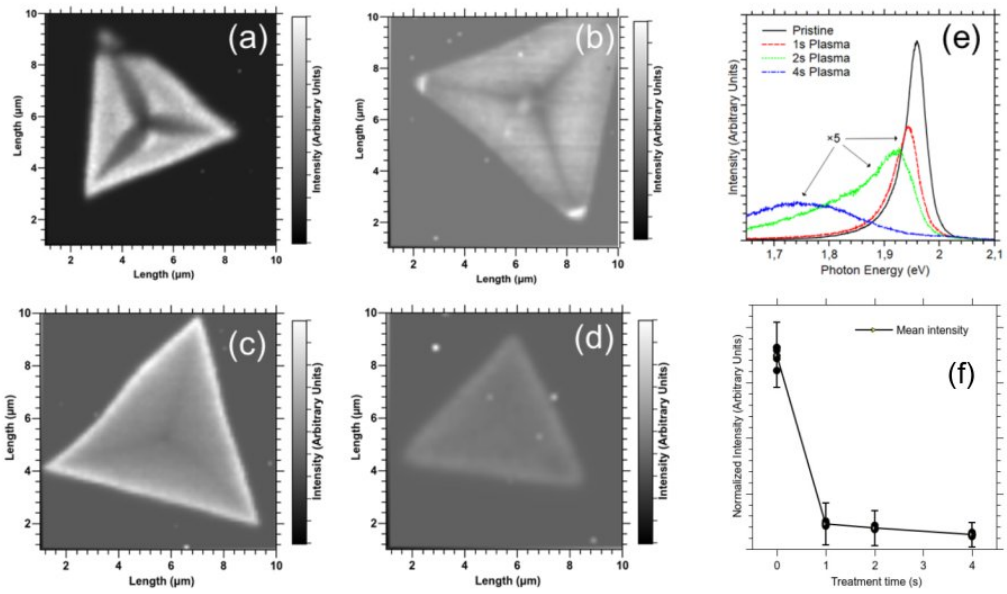

Figure 4.6. (a-d) The progressive loss of PL signal starting from the pristine sample and contrast due to Ar Plasma treatment for 1s, 2s, ad 4s, respectively. After 8s plasma treatment, the PL was fully quenched. (e) An PL peak redshift follows the subsequent signal loss. (f) The mean intensity variation with respect to the treatment time ratio also suggests a strong loss in the PL signal for all measured samples.

Figure 4.6(a-d) shows the PL intensity map of the pristine monolayer WS_2 sample and those submitted to an increasing Ar plasma exposure. The plasma treatment time ranged from 1s to 4s (Figure4.6(b-d), respectively). PL is heavily

quenched due to the plasma treatment. This luminescence loss is expected since the creation of vacancies in the lattice greatly influences both the band structure of the material and the probability of radiative transitions. Also, there is a strong redshift of the main PL peaks from 1.95 eV to 1.80 eV and a broadening of PL, as one can see in Figure 4.6(e). This figure also shows that the PL intensity decreases with increasing plasma exposure time. After 8s plasma treatment, the PL was fully quenched, and therefore it does not appear in Figure 4.6(e). Finally, Figure 4.6(f) shows that the $I_{PL}/I_{si\ Raman}$ ratio, where $I_{si\ Raman}$ is the intensity of the Si Raman peak at 520 cm^{-1}, indicates that the PL signal is lost progressively. These results, combined with Raman and AFM data reported above, indicate that these PL changes are due essentially to the creation of defects in the material. Indeed, this is an average behavior, either considering the normalization of the $PL_{Area}/Raman_{Area}$ or normalizing by its intensity, as seen in Figure 4.6. In this case, five different monolayers crystals were probed for each plasma treatment time. We see that the PL intensity remains the same, within the standard deviation, for all treatment times, which shows that the plasma treatment affects different monolayers rather the same way.

XPS measurements were carried out to determine the chemical environment on pristine and treated WS_2 samples. Figure 4.7 shows the XPS spectra for core levels of the W_{4f} and S_{2p} corresponding to the pristine sample and the plasma-treated one by 8 s. For the pristine sample (Figure 4.7(a)), the peaks at around 33.2 eV and 35.4 eV correspond to W^{4+}. This valence state is associated with WS_2 ($4f_{7/2}$ and $4f_{5/2}$), while 36.2 eV corresponds to $W^{6+,}$ which is the valence state of WO_3, and the peak at 38.5 eV corresponds to WS_2 (W_{5p}). The sulfur sites in the network can be occupied by oxygen atoms, which have as source the precursor of W employed in the synthesis. These atoms are bonded to tungsten atoms (W^{6+}). The peaks at around 163 eV and 164.5 eV (Figure 4.7(b)) correspond to S^{2-}, which is the valence state associated with WS_2 ($2p_{3/2}$ and $2p_{1/2}$). Analysis of the S_{2p} and W_{4f} concentrations provide a W:S ratio of 0.55 ± 0.06, indicating that nearly stoichiometric WS_2 samples were synthesized.

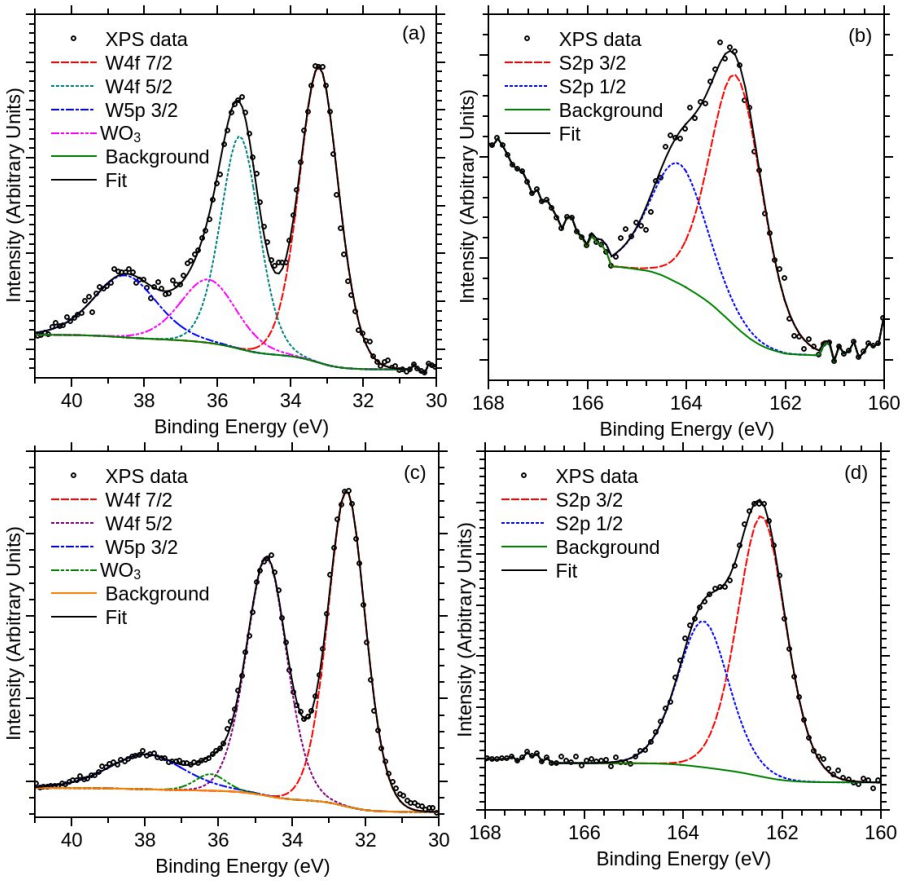

Figure 4.7. XPS spectra for W_{4f} and S_{2p} core levels of both pristine and plasma treatment by 8s samples. (a) and (c) are W_{4f} peaks for samples pristine and 8s-plasma. (b) and (d) are S_{2p} peaks for samples pristine and 8s-plasma, respectively. In (a) and (c), the dashed lines are spin-orbit $4f_{7/2}$ and $4f_{5/2}$ of the W core level. Also, one may see the intensity loss related to WO_3. In (b) and (d), the red and blue dashed lines are split-orbit $2p_{3/2}$ and $2p_{1/2}$ of the S- core level. All- spectra fitting was performed using pseudo-Voigt profile functions and a background type-Shirley function.

When the WS_2 monolayer samples were exposed to Ar plasma for 8s, the XPS spectra (Figure 4.7(c-d)) show that W and S atoms remained essentially with the same valence states. However, two features were observed in the sample: The first one, and the more important, was a decrease in binding energy (a redshift) of ~0.7 eV for both W- and S-core level energies, and the second one was the reduction of the concentration of WO_3. The exfoliated single-layer WS_2 is usually n-type. The defect type for CVD-grown TMDs is dominated by S-vacancies, which n-dopes the material, while W-vacancies p-dopes it [71]. The charge transfer can explain such a redshift to the sample, *i.e.,* the Ar-plasma creates defects (vacancies) that p-doped the material. In this case, one may relate the redshift with

W-vacancies. This is supported by W:S ratio. The analysis of the S_{2p} and W_{4f} concentrations for this sample provides a W:S ratio of 0.44 ± 0.06, suggesting a sulfur-rich surface. The reduction of WO_3 concentration can be explained by preferential sputtering of oxygen compared to S and W.

4.4
N_2 plasma results

Figure 4.8(a) shows the Raman spectra of pristine and treated samples (1s, 2s, and 4s) obtained using a 514.5 nm laser, near resonance energy close to B exciton with absorption peaks at circa 2.4 eV [90,91]. The peak at around 174 cm^{-1} is assigned to a longitudinal acoustic mode near M point in the first Brillouin zone. The LA(M) mode is not present in defect-free structures; however, zone-edge modes are observable through conventional Raman spectroscopy. The momentum conservation condition can be satisfied by the phonon scattering from defects. In that case, the LA(M) phonon is only active when defects are present in the crystal lattice. Therefore, one may study the influence of defects better using excitation energies in the green region in the case of WS_2 as their signal is augmented when the excitation energy close to 2.4 eV is used to amplify the resonant Raman response [50]. In this case, the LA(M) phonon may be used as a figure of merit to infer a higher density of defects in the lattice indirectly. There is a constant evolution in the intensity of the prominent LA(M) phonon upon treatment time, as shown in Figure 4.8(b).

The Raman main modes are also seen in this range: the in-plane acoustic 2LA(M) at ~350 cm^{-1}, in-plane E_{2g} at around 355 cm^{-1}, and the out-of-plane A_{1g} mode close to 418 cm^{-1}. It is clear the effect of the plasma treatment, which affects these phonons, slightly changing its intensity, full width at half maximum (FWHM), and area (Figure 4.8(a) and Table 1). This implies that the plasma treatment is creating defects in the lattice and implanting nitrogen species, as will be discussed later when the XPS data will be presented. The most crucial point to highlight is the redshift of peaks 2LA(M), E_{2g}, and A_{1g} due to the presence of nitrogen in the sample.

In Figure 4.8(c), both the intensity and area of the LA(M) are plotted as functions of the treatment time. The evolution of the LA(M) mode shows a steady increase in both parameters, showing that damping mechanisms, such as phonon-phonon scattering lifetimes, and the increase in the number of scattering centers,

are being progressively affected by the plasma treatment time. These results suggest that the system is slowly losing its crystallinity after longer periods of plasma bombardment. Evidence of such change is the fact that the intensity of LA(M) mode compared to adjacent modes at ~ 190 cm^{-1} and ~ 215 cm^{-1} show a progressive increase in intensity as a function of the treatment time.

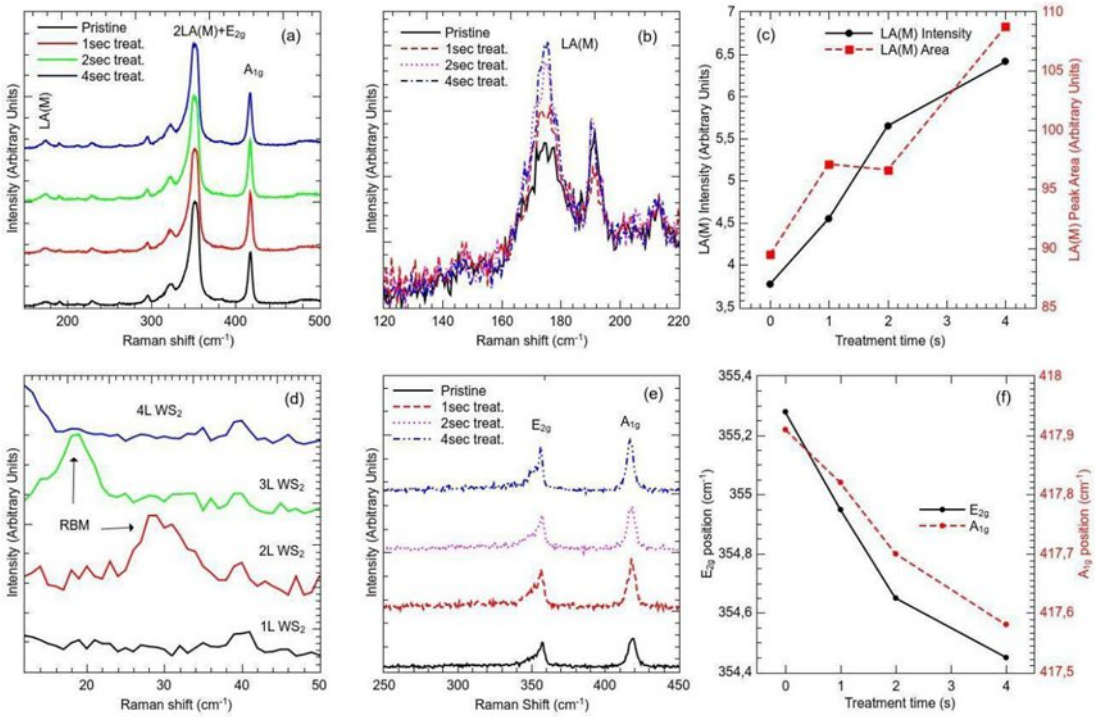

Figure 4.8. Spectra shown in figures (a-c) were obtained using a 514,5 nm laser, while data show in figures (d-f) wee obtained with a 488 nm laser. (a) Raman spectra of pristine and treated samples. (b) LA(M) spectra for pristine and treated samples. This mode is directly affected by the treatment. Its intensity increases progressively with plasma exposition time. (c) LA(M) Intensity and area behavior graph as functions of the treatment time. (d) Identification of radial breathing modes and discrimination of the number of WS_2 layers. (e) Raman spectra of pristine and treated WS_2 samples. (f) E_{2g} and A_{1g} shift due to the plasma surface treatment.

Table 4.1. Raman deconvolution parameters of the spectra are shown in Figures 4.8(a) and 4.8(b). One can see the evolution of the E_{2g} and A_{1g} due to surface treatment. The area is in arbitrary units.

Sample	LA(M)			2LA(M)			E_{2g}			A_{1g}		
	Position	FWHM (cm^{-1})	Area	Position	FWHM (cm^{-1})	Area	Position	FWHM (cm^{-1})	Area	Position	FWHM (cm^{-1})	Area
0s	174,8	7,5	89	350.5	4.7	1148	355.3	2.3	384	417.9	2.4	387
1s	174.8	6.8	97	350.3	4.7	1031	355.0	2.8	418	417.8	2.4	404
2s	174.2	5.9	109	345.0	4.4	1015	354.7	2.4	359	417.7	2.4	395
4s	174.7	5.4	110	349.6	4.3	935	354.5	2.3	365	417.6	2.6	359

To obtain Raman spectra away from strongly resonant A, B, and C excitons and better analyze both E_{2g} and A_{1g} modes, the 488 nm excitation laser is used. Figure 4.8(e) shows the main heavily quenched 2LA(M), and prominent E_{2g} and A_{1g} phonons as features. It is seen that the treatment of the samples causes a small position shift of the characteristic E_{2g} and A_{1g} phonons. This shift, when one compares the pristine and the samples treated for 4s, is beyond the system's experimental error, as can be seen in Figure 4.8(f). This can be seen because of the strong suppression of the double-resonant 2LA(M) phonon under such excitation energy (2.54 eV, i.e., 488 nm). This shift can show a slight change in the lattice constants, which affects the band structure of the material [92] or p-doping due to nitrogen incorporation into the crystal lattice.

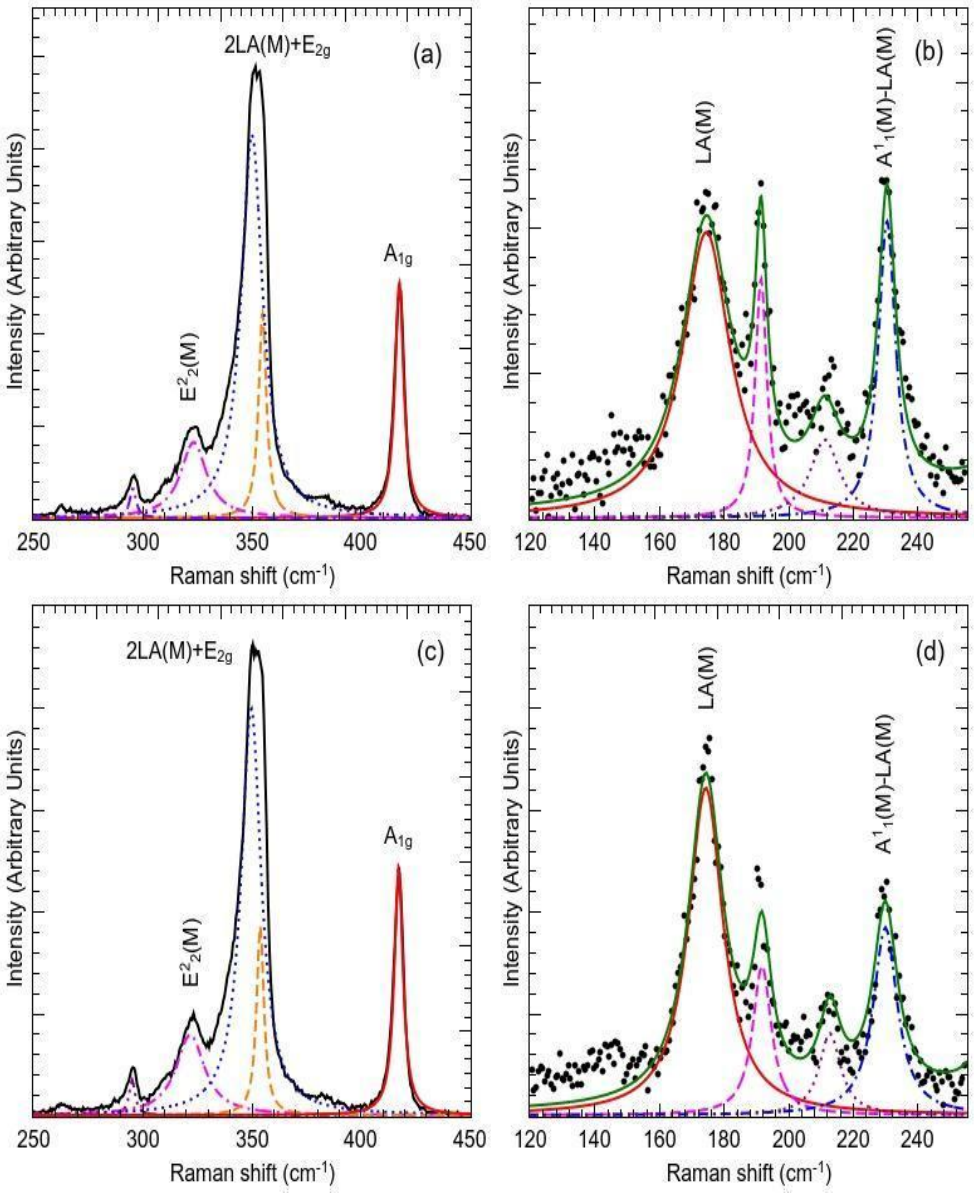

Figure 4.9. Deconvolution of Raman spectra of pristine and treated samples excited with 514.5nm laser. (a) and (b): Deconvolution of peaks related to the pristine sample. (c) and (d) Deconvolution of peaks related to the 4s plasma-treated sample. One may see the LA(M) phonon intensity increase due to treatment. The E_{2g} shifted from 355.3 cm^{-1} to 354.5 cm^{-1}.

As reported in [88, 93], one may see an extra Raman mode convoluted with the A_{1g} phonon and another peak at ~ 440 $cm^{-1,}$ which appears for a remarkably high density of defects. On the other hand, close to bandgap measurements show that the presence of extra WS_2 layers causes a clear split in the A_{1g}, as previously reported in reference [21]. Low-frequency Raman

measurements were used to correctly identify monolayer samples by identifying the areas without the presence of radial breathing modes and shear modes to avoid such ambiguities in the interpretation of the spectra, i.e., the necessity in establishing the number of layers of the samples, hence ruling out any Raman peak shift due to the presence of extra layers, characteristic of multilayered samples (Figure4.8 (d)). Taking this under consideration, the observed shifts in Raman peaks positions are only caused by nitrogen plasma treatment.

From the peak LA(M) in Figures 4.8(a), 4.8(b), and Figure 4.9(b), the pristine samples of WS_2 obtained by CVD are not defect-free. In this case, the defects can be associated with S-vacancies. Figure 4.9 shows the deconvolution of Raman features of the pristine (Figures 4.9(a) and 4.9(b)) and 4s (Figures 4.9(c) and (d)) treated samples, respectively. The spectra were obtained using a 514.5 nm excitation laser. The FWHM of E_{2g} peak stays nearly constant even for the longer plasma treatment, suggesting that the possible nitrogen incorporation cannot be associated with the weakening of the E_{2g} phonon. On the other hand, the E_{2g} peak shifts about 1 cm^{-1} from the pristine sample to the 4s treated one, suggesting p-doping of the material. The LA(M)/[A^1_1(M)-LA(M)] intensity ratio varies from 0.9 to 1.7. This behavior was consistent for several spectra taken from different points of the sample and suggests that this ratio may show a progressive increase in defects density, scattering centers, caused by nitrogen presence in the crystal lattice.

The photoluminescence in TMD monolayers is dominated by the recombination of electrons in the conduction band with holes in the spin-orbit split valence bands. There are two distinct emission features: X^0(ground state exciton recombination) and X^T, which are due to bound states of two electrons and a hole or one electron and two holes, known as trions. Taking this into account, along with the observed asymmetry, we have assigned two Lorentzian peaks for the curve, being the lower energy and intensity, one assigned to negatively charged trions [94]. Figure 4.10(a) and 4.10(b) shows the fitted curves of the X^0 and X^T peaks for pristine and the sample treated for 4s. The spectra were normalized by the intensity of the first-order Raman Si peak instead of the A_{1g} peak of WS_2 to compare the PL intensities correctly, independent of the CCD photo-response, as its value is essentially constant on all points of the map. The photoluminescence arising from the direct radiative recombination of electron−hole pairs is not strongly

red-shifted due to the treatment, as was shown in similar earlier investigation [27] when WS_2 samples were irradiated with low energy atomic nitrogen beams. This confirms that the band structure of the materials is not radically affected. Rather, nitrogen impurities increase the probability amplitude of the electron-hole radiative recombination, improving the emission intensity.

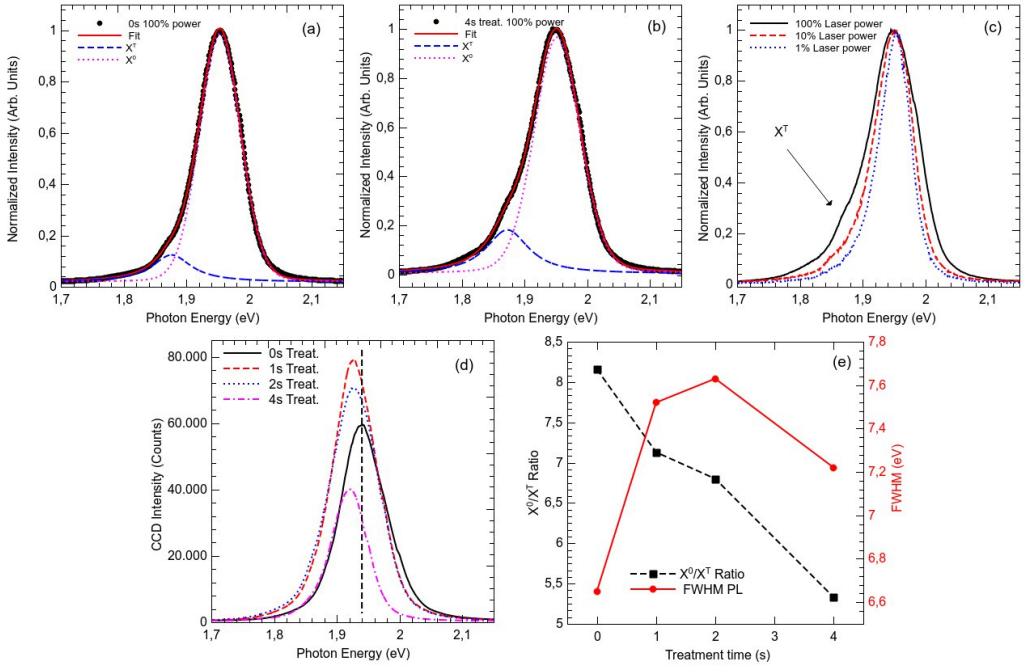

Figure 4.10. (a) and (b) are the deconvolutions of the X^T and X^0 peaks in the pristine and 4s treated samples (2 mW). The X^0 and X^T line shape and increase with the treatment time. (c) PL peak asymmetry evolution of the 4s plasma-treated sample with respect to the laser power is clearly shown. One may observe the X^T shoulder evolution in the figure. Also, the same behavior is observed in the other treated samples. (d) PL intensity enhancement and redshift observed in the sample. The PL peak intensity increased as much as 34.1% from pristine to 1s treated WS_2 monolayers on average. (e) X^0/X^T Ratio and FWHM of the full PL peaks.

Also, X^T exciton shows a dependence on laser power, as well as the treatment time. The evolution of the PL peak asymmetry for the sample treated for four seconds is shown in Figure 4.10(c). One can see that this contribution evolves as a function of the laser power, as was reported in the literature. The asymmetry is less evident in the samples treated for 1s and 2s. However, at the highest laser power available in our instrument (NT-MDT SPECTRA), this asymmetry increases compared to the PL spectra excited with lower laser powers.

Figure 4.10(d) shows the PL intensity effect of increasing nitrogen plasma exposure on the PL of single-layer WS_2. The plasma exposure duration ranged from 0 to 4s. It is important to note that Figure 4.10(d) spectra were taken with the same configuration, showing that the light emission is higher for the samples treated for 1s and 2s. Also, after a first improvement of the intensity of emission, the emission intensity of 4s treated samples is lower when compared with the pristine and 1s, and 2s treated WS_2 monolayers. Also, the emitting light was weakly red-shifted. This shift can be attributed to a substantial increase in the density of defects for the longer 4s plasma treatment. The observed PL redshift in most direct-gap semiconductors originates mainly due to discrete defect states inside the bandgap. Our XPS data suggests that indeed, N is incorporated into the lattice. Hence, the impurity energy levels will form in the electronic bandgap, and the recombination of excited electron-hole pairs will emit photons with smaller energies compared to those emitted by pristine samples. The evolution of the PL peak parameters may be appreciated further in Figure 4.10(e) and Table 2, where the A/X^T ratio measured at 100% laser power also increases as a function of the treatment time.

Table 2. PL parameters related to the measured samples with 100% laser power.

Treatment Time (s)	FWHM (10^{-2} eV)	CCD means Intensity (10^3 Counts)	Peak Energy (eV)	X^0/X^T Ratio
0	6.65	59	1.94	8.16
1	7.52	79	1.92	7.13
2	7.63	72	1.92	6.82
4	7.22	32	1.91	5.33

One of the main problems dealing with the PL response of WS_2 crystals is the progressive inward loss of signal intensity of monolayer structures. This is a challenge since the behavior is due to the higher concentrations of defects inside the triangular-shaped structures [95]. Figures 4.11(a) and (b) show an atypical PL response for the samples in this work, which is remarkably uniform, unlike typical CVD-grown WS_2 monolayers. This indeed may be because of sodium traces within the reactor, which improves the photo-response of the monolayers, the origin of this contaminant being a previous synthesis in the same reactor [93]. With increasing plasma exposure time up to two seconds, the emission intensity is improved, and the luminescence uniformity is still present. As a comparison, the

photoluminescence emission distribution as a function of the treatment time of a different mapped WS_2 is shown in Figure 4.11(c), where an emission intensity is enhanced by 34.1% for treatment times up to two seconds.

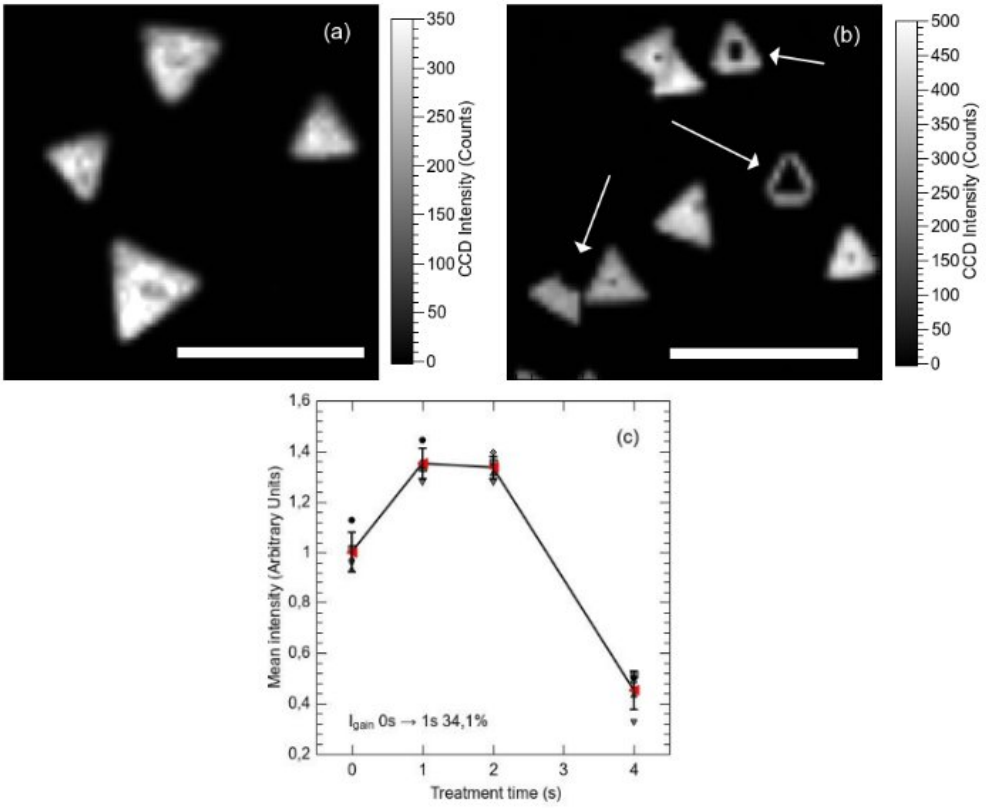

Figure 4.11. (a) PL map of the 4s treated monolayer triangles. It is possible to see the relative emission uniformity of the sample. (b) PL map of several pristine WS_2 monolayer triangles, bilayer regions are pointed by arrows in the figure. (c) The average intensity of mapped different WS_2 monolayer samples as a function of time. The intensity gain due to 1s treatment time was 34.1% compared to the average of intensity values measured on pristine. The scale bar in (a) and (b) is 30 µm.

In Figure 4.12(a) and 4.12(b), we show the XPS spectra related to core levels of the W_{4f} and S_{2p} obtained from pristine samples, while in Figure 4.12(c) and 4.12(d), the spectra were taken from samples treated for 1s. See also Table 3 for both W_{4f} and S_{2p} energy values obtained by fitting the high-resolution XPS spectra using CasaXPS. In this fitting, the splitting of spin-orbital components (in both W_{4f} and S_{2p}) and loss features of W_{5p} were used. The spectrum shifts towards low binding energies for treated samples. The W_{4f} spectrum in Figure 4.12(a) is composed of W atoms bonded to S atoms, by far the more important contribution,

and shows the presence of residual WO_3. In Figure 4.12(c), nitrogen is incorporated in the crystal lattice since W atoms bonded to N are present in the W_{4f} spectrum. The redshift observed for both S and W peaks after the plasma exposition can be attributed to the substitution of S by N in the WS_2 lattice, as suggested previously by first-principle calculations that showed that N at S sites is energetically favored when compared to all other possibilities of nitrogen incorporation [96].

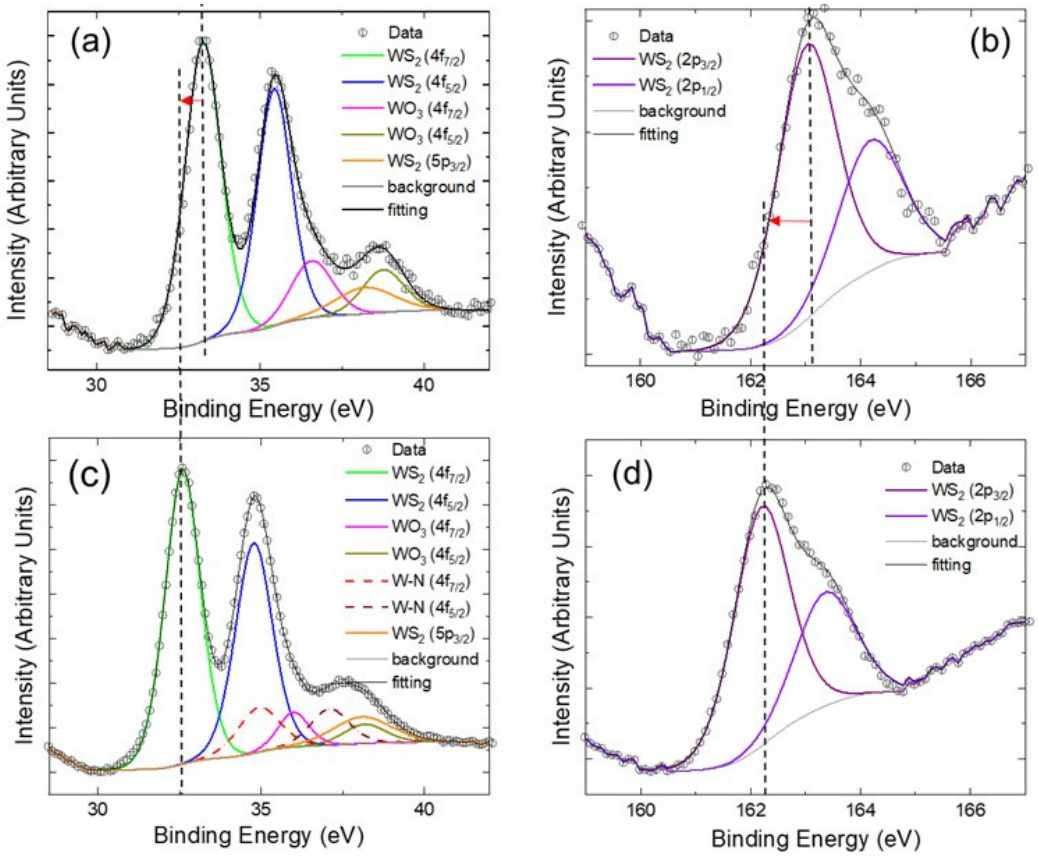

Figure 4.12. (a) and (b) show the XPS spectra related to core levels of the W_{4f} and S_{2p} for pristine samples, while (c) and (d) are the spectra compared to samples treated for 1s. There is a clear shift towards low binding energies (0.8 eV) for treated samples, as it is shown by the dashed line and red arrow in the figure. Nitrogen is incorporated in the crystal structure, as seen in (c) since W atoms bonded to N are present in the W_{4f} spectrum.

To analyze the observed charge transfer in XPS spectra, the valence band maximum (VBM) of these films was determined by the linear extrapolation method (Linear extrapolation means creating a tangent line at the end of the known data and extending it beyond a given limit), as shown in Figure 4.13(a) and 4.14(b). It is shown the positions of the valence band maximum (VBM) for both pristine samples

and the sample treated for 1s. The change in position of VBM, a shift to lower binding energy, suggests that the Fermi level is approaching the VBM, a clear indication of p-type doping due to nitrogen incorporation as a result of plasma treatment [97], already suggested by Raman results.

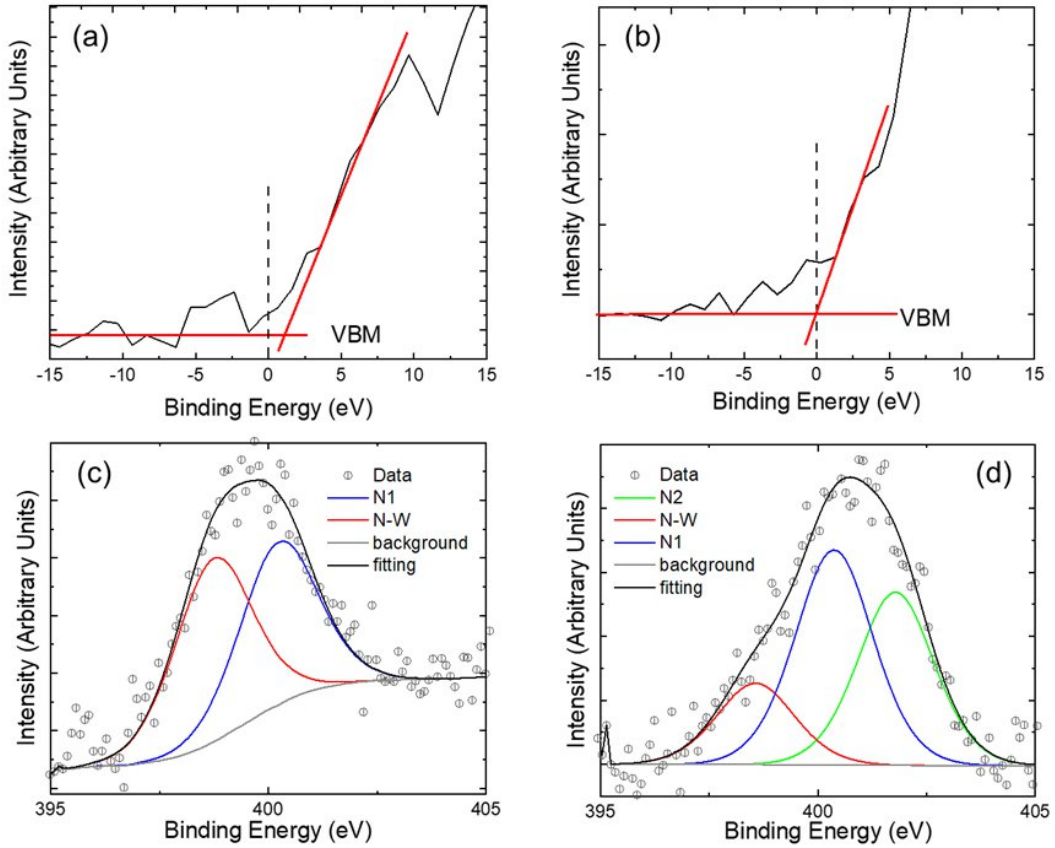

Figure 4.13. (a) and (b) show the VBM for pristine samples and the sample treated for 1s. The observed shift to lower binding energies shows that the Fermi level indicates p-type doping due to nitrogen incorporation in the structure. (c), (d) show the spectra of the N_{1s} core level for 1s, and 4s, respectively. N1-peak is associated with the absorbed N-containing gaseous forms, and to O-N(-Si)$_2$ environment, and N_2-peak is attributed to oxidized nitrogen cations (N-SiO_2).

XPS analyzed the nitrogen chemical environment, and the spectra of the N_{1s} core level are shown in Figures 4.13(c) and (d) for different treatment times. In Figure 4.13(c), the spectrum of the treated sample for 1s reveals the presence of a broad peak centered at around 398.7 eV in the upper range of the usually reported values for W-N chemical bonds [98]. We cannot discard a contribution of the nitrogen bonded to silicon atoms. The energy for Si-N bonds in nitrogen plasma treated SiO_2 surfaces can be found between 397.4–398.4 eV, depending on the

nitrogen concentration [99]. However, it is expected that this contribution became more important for longer treatment times when the integrity of the WS_2 was lost. A contribution at 400.2 eV (N1-peak) could be related to the absorbed N-containing gaseous forms and O-N(-Si)$_2$ chemical environment. [98,99], became the dominant peak with N-peak associated with oxidized nitrogen cations at 402.5 eV for the sample treated for 4s, as shown in Figure 4.13(d). In Table 3, we show the total relative composition of the samples, showing the increase of N content upon longer treatment times. This increase occurs at the expense of S, removed from the lattice by the plasma-surface interaction, as it is shown in the table. On the contrary as was observed for Ar plasma treatment we do not expected W sputtering since N plasma is a reactive plasma, indicated by the presence of W-N bonds in the spectra of treated samples. In fact, Ar plasma effects are essentially controlled by binary collisions and, because of the higher mass of Ar when compared to N, the ballistic sputtering of W atoms in this atmosphere is more probable than in the case of N plasma.

Table 3. Relative atomic concentration.

Sample	W/S Ratio	Relative concentration at the W peak			
		W-S	W-N	WO_3	W-S ($5p_{3/2}$)
0s	0.58	77	-	17	6
1s	0.47	73	13	8	6
4s	0.51	67	18	8	7

AFM images of pristine and nitrogen plasma treated WS_2 crystal flakes are shown in Figures 4.14(a) and (b). The scan area is 100 μm^2. In the image, we can see the color contrast between the substrate (SiO_2/Si) and the triangular WS_2 flakes. Changes in the morphology are seen directly from AFM images. Figure 4.14(c) shows an evolution of the roughness as a function of treatment time. The roughness is increased to 1.2nm after four seconds of plasma treatment. The lower luminescence response may be related to the observed increase in roughness since the treatment degrades the monolayers.

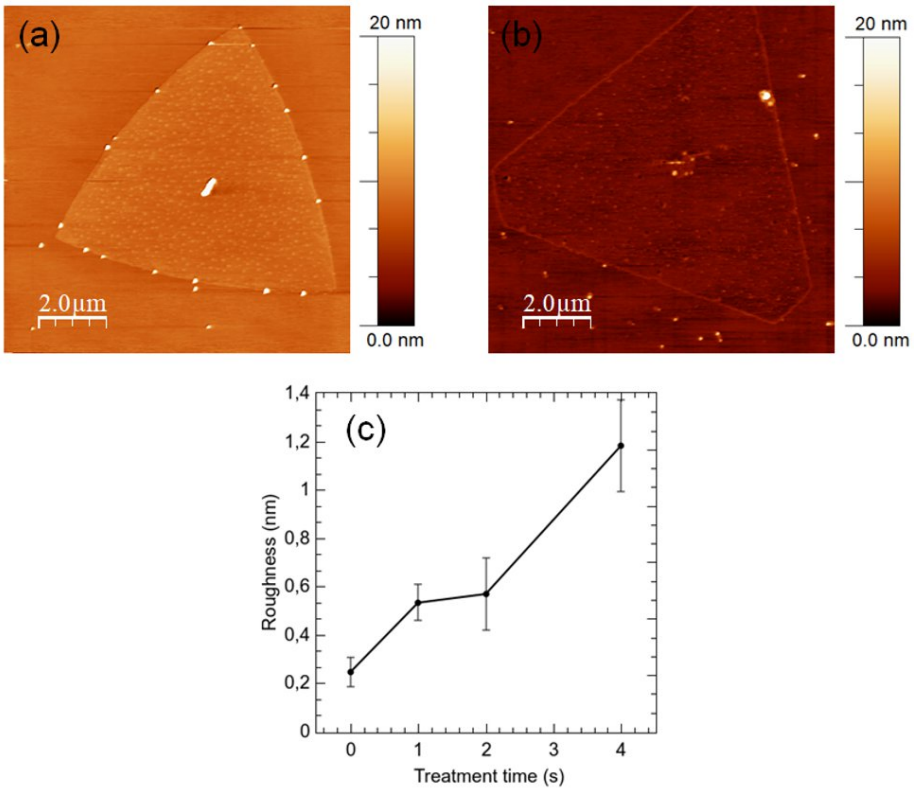

Figure 4.14. AFM topography of WS_2: (a) Pristine and (b) N_2 plasma exposure for 4 seconds. (c) Roughness as a function of treatment time.

Further, the increased but similar roughness in samples treated for one and two seconds also relates to the observed similar photoemission intensity of these samples. In this case, it is implied that after this time threshold, i.e., for longer treatment times, the weaker photoluminescence emission of samples is due to the surface degradation caused by the plasma bombardment rather than by the incorporation of nitrogen ions in the lattice. XPS results showed that for 4s treatment, the N-containing gases are the main contribution to the core level N*1s* spectrum. These results, combined with AFM measurements, suggest that the rough surface of the sample traps gas molecules. Compared with the roughness of Ar treated samples, the roughness achieved after 4s of N plasma treatment is similar within experimental errors. However, the roughness of Ar treated sample reached this value after only 2s of exposition to the plasma. These results indicate that the deterioration of the sample surface, as measured by AFM, can be correlated to the observed PL reduction.

5
Conclusions

The effective and reliable synthesis of TMDs at sufficiently large scales creates a need to standardize the physical properties of TMD materials. Indeed, the industry will define and differentiate, given the methods of characterization, good and bad substrates for a subsequent device fabrication for a given purpose. Also, the required modification in a production line should yield, ideally, identical properties for many individual crystals. One of several material modifications approaches that is controllable enough to modify these materials is the low-energy surface plasma treatment.

Concerning the first point, the observed splitting of the A_{1g} phonon under close to resonance Raman condition may be used to discriminate WS_2 monolayers from few-layered crystals as well as bulk structures that were grown by CVD unequivocally. Leveraging this unique property makes it easy to correctly identify WS_2 stacks relying upon a specific spectral feature independent of the substrate or energy-dispersive. Also, the observed A_{1g} - A^*_{1g} splitting is beyond most systems margin of error (~2 cm^{-1}), where it is observed using a laser excitation wavelength of 647 nm, a band split of up to ~5 cm^{-1} for 3L WS_2, and a constant increase of the A_{1g}/A^*_{1g} intensity ratio as a function of the number of layers.

Also, the Ar plasma treatment creates defects in the crystal lattice, which results in the strong quenching and redshift of the PL spectra. The intensity variation of LA(M) mode and the broadening and 2LA(M) Raman modes indicate the material has a higher defect density for longer treatment times. Cross-polarized Raman measurements also showed a relevant LA(M) mode increase due to surface treatment. Our experiments showed that the PL was completely suppressed for treatments longer than 8 seconds confirming the Raman signal degradation as a function of the treatment time. In other words, one may modify the electronic properties by exposing WS_2 monolayers to low-power Ar-plasma for a few seconds.

Moreover, the results support that the WS_2 structures that underwent the nitrogen plasma treatment showed an improvement in their photoluminescence response. Raman spectroscopy results points to an increase in the density of

defects as the LA(M) phonon shows an increase in its intensity. Moreover, the LA(M)/A_1(M)-LA(M) intensity ratio may be used as a figure of merit to show an increase in the density of defects in the lattice. On the other hand, XPS measurements indicate the incorporation of nitrogen in the crystal lattice, a redshift of the core level W_{4f} and S_{2p} spectra, and a change in the VBM, revealing the p-doping of WS_2 monolayers is confirmed by the redshift observed on the Raman spectra. The p-type doping of WS_2 structures is a necessary step towards the fabrication of p-n homojunction based devices. Finally, main result of this thesis is the observed photoemission intensity emission for samples treated for 1s and 2s were enhanced by as much as 34.1%, thus showing that this low-cost, fast, and straightforward treatment process is a reliable and practical technique to improve further the characteristics of optoelectronic devices based on WS_2 monolayer structures.

6
References

1 CHOI, Wonbong et al. Recent development of two-dimensional transition metal dichalcogenides and their applications. **Materials Today**, v. 20, n. 3, p. 116-130, 2017.

2 NOVOSELOV, K. S. et al. 2D materials and van der Waals heterostructures. **Science**, v. 353, n. 6298, 2016.

3 JARIWALA, Deep et al. Emerging device applications for semiconducting two-dimensional transition metal dichalcogenides. **ACS nano**, v. 8, n. 2, p. 1102-1120, 2014.

4 LOTSCH, Bettina V. Vertical 2D heterostructures. **Annual Review of Materials Research**, v. 45, p. 85-109, 2015.

5 MANZELI, Sajedeh et al. 2D transition metal dichalcogenides. **Nature Reviews Materials**, v. 2, n. 8, p. 17033, 2017.

6 NOVOSELOV, Kostya S. et al. Electric field effect in atomically thin carbon films. **Science**, v. 306, n. 5696, p. 666-669, 2004.

7 MCCREARY, Amber et al. Distinct photoluminescence and Raman spectroscopy signatures for identifying highly crystalline WS_2 monolayers produced by different growth methods. **Journal of Materials Research**, v. 31, n. 07, 2016.

8 SUSARLA, Sandhya et al. Quaternary 2D transition metal dichalcogenides (TMDs) with tunable bandgap. **Advanced Materials**, v. 29, n. 35, p. 1702457, 2017.

9 UGEDA, Miguel M. et al. Giant bandgap renormalization and excitonic effects in a monolayer transition metal dichalcogenide semiconductor. **Nature materials**, v. 13, n. 12, p. 1091-1095, 2014.

10 WANG, Yanlong et al. Strain-induced direct–indirect bandgap transition and phonon modulation in monolayer WS_2. **Nano Research**,

v. 8, n. 8, p. 2562-2572, 2015.

11 LU, Ning et al. MoS_2/MX_2 heterobilayers: bandgap engineering via tensile strain or external electrical field. **Nanoscale**, v. 6, n. 5, p. 2879-2886, 2014.

12 HUO, Nengjie; YANG, Yujue; LI, Jingbo. Optoelectronics based on 2D TMDs and heterostructures. **Journal of Semiconductors**, v. 38, n. 3, p. 031002, 2017.

13 WANG, Shanshan et al. Shape evolution of monolayer MoS_2 crystals grown by chemical vapor deposition. **Chemistry of Materials**, v. 26, n. 22, p. 6371-6379, 2014.

14 LI, Xiao-Lin; GE, Jian-Ping; LI, Ya-Dong. Atmospheric Pressure Chemical Vapor Deposition: An Alternative Route to Large-Scale MoS_2 and WS_2 Inorganic Fullerene-like Nanostructures and Nanoflowers. **Chemistry–A European Journal**, v. 10, n. 23, p. 6163-6171, 2004.

15 CHUNG, J.-W.; DAI, Z. R.; OHUCHI, F. S. WS_2 thin films by metal organic chemical vapor deposition. **Journal of crystal growth**, v. 186, n. 1-2, p. 137-150, 1998.

16 SHAW, Jonathan C. et al. Chemical vapor deposition growth of monolayer $MoSe_2$ nanosheets. **Nano Research**, v. 7, n. 4, p. 511-517, 2014.

17 NAN, Haiyan et al. Recent advances in plasma modification of 2D transition metal dichalcogenides. **Nanoscale**, v. 11, n. 41, p. 19202-19213, 2019.

18 SUN, Linfeng et al. Plasma modified MoS_2 nanoflakes for surface enhanced Raman scattering. **Small**, v. 10, n. 6, p. 1090-1095, 2014.

19 ZHAO, Wei et al. Strong photoluminescence enhancement of MoS_2 monolayer via low-power Ar/O2 plasma treatment. **Materials Letters**, v. 235, p. 129-132, 2019.

20 KANG, Narae et al. Photoluminescence quenching in single-layer MoS_2 via oxygen plasma treatment. **The Journal of Physical Chemistry C**, v. 118, n. 36, p. 21258-21263, 2014.

21 DO NASCIMENTO BARBOSA, André et al. Luminescence enhancement and Raman characterization of defects in WS_2 monolayers treated with low-power N2 Plasma. **Applied Surface Science**, p. 147685, 2020.

22 JADWISZCZAK, Jakub et al. Oxide-mediated recovery of field-effect mobility in plasma-treated MoS_2. **Science advances**, v. 4, n. 3, p. eaao5031, 2018.

23 BOZHEYEV, Farabi et al. Photoluminescence quenching of WS_2 nanoflakes upon Ga ion irradiation. **Journal of Luminescence**, v. 217, p. 116786, 2020.

24 DANDU, Medha et al. Strong Single-and Two-Photon Luminescence Enhancement by Nonradiative Energy Transfer across Layered Heterostructure. **ACS nano**, v. 13, n. 4, p. 4795-4803, 2019.

25 TANG, Baoshan et al. Direct n-to p-type channel conversion in monolayer/few-layer WS_2 field-effect transistors by atomic nitrogen treatment. **ACS nano**, v. 12, n. 3, p. 2506-2513, 2018.

26 HUANG, Sheng-Feng et al. First-principles calculation of the electronic properties of graphene clusters doped with nitrogen and boron: analysis of catalytic activity for the oxygen reduction reaction. **Physical Review B**, v. 80, n. 23, p. 235410, 2009.

27 JIANG, Jianfeng et al. A facile and effective method for patching sulfur vacancies of WS_2 via nitrogen plasma treatment. **Small**, v. 15, n. 36, p. 1901791, 2019.

28 WANG, Ziqian et al. Unveiling three-dimensional stacking sequences of 1T phase MoS_2 monolayers by electron diffraction. **ACS nano**, v. 10, n. 11, p. 10308-10316, 2016.

29 DAI, Zhongwei et al. Surface structure of bulk 2H- MoS_2 (0001) and exfoliated suspended monolayer MoS_2: A selected area low energy electron diffraction study. **Surface Science**, v. 660, p. 16-21, 2017.

30 JOENSEN, P. et al. A study of single-layer and restacked MoS_2 by X-ray diffraction and X-ray absorption spectroscopy. **Journal of Physics C: Solid State Physics**, v. 20, n. 26, p. 4043, 1987.

31 HOUSSA, Michel; DIMOULAS, Athanasios; MOLLE, Alessandro (Ed.). **2D materials for nanoelectronics**. CRC Press, 2016.

32 CALANDRA, Matteo. Chemically exfoliated single-layer MoS_2: Stability, lattice dynamics, and catalytic adsorption from first principles. **Physical Review B**, v. 88, n. 24, p. 245428, 2013.

33 CHEN, Shao-Yu et al. Helicity-resolved Raman scattering of MoS_2 $MoSe_2$, WS_2, WSe_2 atomic layers. **Nano letters**, v. 15, n. 4, p. 2526-2532, 2015.

34 SOURISSEAU, C. et al. Second-order Raman effects, inelastic neutron scattering and lattice dynamics in 2H- WS_2. **Chemical physics**, v. 150, n. 2, p. 281-293, 1991.

35 VIRŠEK, Marko et al. Raman scattering of the MoS_2 and WS_2single nanotubes. **Surface science**, v. 601, n. 13, p. 2868-2872, 2007.

36 STAIGER, Matthias. Vibrational properties of low-dimensional inorganic layered materials. 2017.

37 ZHANG, Jing et al. Observation of strong interlayer coupling in MoS_2/ WS_2 heterostructures. **Advanced Materials**, v. 28, n. 10, p. 1950-1956, 2016.

38 ZHAO, Xiao-Miao et al. Pressure effect on the electronic, structural, and vibrational properties of layered 2 H− $MoTe_2$. **Physical Review B**, v. 99, n. 2, p. 024111, 2019.

39 TAN, Qing-Hai et al. Observation of forbidden phonons, Fano

resonance and dark excitons by resonance Raman scattering in few-layer WS2. **2D Materials**, v. 4, n. 3, p. 031007, 2017.

40 OTTAVIANO, L. et al. Mechanical exfoliation and layer number identification of MoS_2 revisited. **2D Materials**, v. 4, n. 4, p. 045013, 2017.

41 ZHANG, Xin et al. Phonon and Raman scattering of two-dimensional transition metal dichalcogenides from monolayer, multilayer to bulk material. **Chemical Society Reviews**, v. 44, n. 9, p. 2757-2785, 2015.

42 WANG, Yanlong et al. Strain-induced direct–indirect bandgap transition and phonon modulation in monolayer WS_2. **Nano Research**, v. 8, n. 8, p. 2562-2572, 2015.

43 KLOTS, A. R. et al. Probing excitonic states in suspended two-dimensional semiconductors by photocurrent spectroscopy. **Scientific reports**, v. 4, p. 6608, 2014.

44 SAITO, Riichiro et al. Raman spectroscopy of transition metal dichalcogenides. **Journal of Physics: Condensed Matter**, v. 28, n. 35, p. 353002, 2016.

45 MILLARD, Toby Severs et al. Large area chemical vapour deposition grown transition metal dichalcogenide monolayers automatically characterized through photoluminescence imaging. **npj 2D Materials and Applications**, v. 4, n. 1, p. 1-9, 2020.

46 GUTIÉRREZ, Humberto R. et al. Extraordinary room-temperature photoluminescence in triangular WS_2 monolayers. **Nano letters**, v. 13, n. 8, p. 3447-3454, 2013.

47 SPLENDIANI, Andrea et al. Emerging photoluminescence in monolayer MoS_2. **Nano letters**, v. 10, n. 4, p. 1271-1275, 2010.

48 ZHANG, Fu et al. Carbon doping of WS_2 monolayers: Bandgap reduction and p-type doping transport. **Science advances**, v. 5, n. 5, p. eaav5003, 2019.

49 BARBOSA, A. N. et al. Straightforward identification of monolayer WS_2 structures by Raman spectroscopy. **Materials Chemistry and Physics**, v. 243, p. 122599, 2020.

50 LI, Jiake et al. Atypical defect-mediated photoluminescence and resonance raman spectroscopy of monolayer WS_2. **The Journal of Physical Chemistry C**, v. 123, n. 6, p. 3900-3907, 2019.

51 KERSSEMAKERS, J.; DE HOSSON, J. Th M. Atomic force microscopy imaging of transition metal layered compounds: A two-dimensional stick–slip system. **Applied physics letters**, v. 67, n. 3, p. 347-349, 1995.

52 LUCKEY, George W. Introduction to Solid State Physics. **Journal of the American Chemical Society**, v. 79, n. 12, p. 3299-3299, 1957.

53 REZENDE, Sergio Machado. **Materiais e dispositivos eletrônicos**. Editora Livraria da Física, 2004.

54 HE, Zuyun et al. Defect engineering in single-layer MoS_2 using heavy ion irradiation. **ACS applied materials & interfaces**, v. 10, n. 49, p. 42524-42533, 2018.

55 LEE, Chanwoo et al. Unveiling defect-related Raman mode of monolayer WS_2 via tip-enhanced resonance Raman scattering. **ACS nano**, v. 12, n. 10, p. 9982-9990, 2018.

56 ROSENBERGER, Matthew R. et al. Electrical characterization of discrete defects and impact of defect density on photoluminescence in monolayer WS_2. **ACS nano**, v. 12, n. 2, p. 1793-1800, 2018.

57 JORIO, Ado et al. **Raman spectroscopy in graphene related systems**. John Wiley & Sons, 2011.

58 BASSALO, José Maria Filardo. **Eletrodinâmica clássica**. Editora Livraria da Física, 2007.

59 MAHON, José Roberto Pinheiro. **Mecânica Quântica:**

desenvolvimento contemporâneo com aplicações. LTC, 2011.

60 KITTEL, Charles. **Introdução À Física Do Estado Sólido** . Grupo Gen-LTC, 2000.

61 DEVREESE, Jozef T.; KUNZ, Albert Barry; COLLINS, Thomas C. **Elementary Excitations in Solids, Molecules, and Atom**. Springer Science & Business Media, 2013.

62 LEE, Jae-Ung; CHEONG, Hyeonsik. Resonance Raman effects in transition metal dichalcogenides. **Journal of Raman Spectroscopy**, v. 49, n. 1, p. 66-75, 2018.

63 QIU, Diana Y.; FELIPE, H.; LOUIE, Steven G. Optical spectrum of MoS_2: many-body effects and diversity of exciton states. **Physical review letters**, v. 111, n. 21, p. 216805, 2013.

64 ZHAO, Weijie et al. Evolution of electronic structure in atomically thin sheets of WS_2 and WSe_2. **ACS nano**, v. 7, n. 1, p. 791-797, 2013.

65 CARVALHO, Bruno R.; PIMENTA, Marcos A. Resonance Raman spectroscopy in semiconducting transition-metal dichalcogenides: basic properties and perspectives. **2D Materials**, 2020.

66 MALARD, L. M. et al. Raman spectroscopy in graphene. **Physics reports**, v. 473, n. 5-6, p. 51-87, 2009.

67 LI, Yilei et al. Measurement of the optical dielectric function of monolayer transition-metal dichalcogenides: MoS_2, $MoSe_2$, WS_2, and WSe_2. **Physical Review B**, v. 90, n. 20, p. 205422, 2014.

68 FAZZIO, Adalberto; WATARI, Kazunori. Introdução à Teoria de Grupos aplicada em moléculas e sólidos. **Santa Maria: UFSM**, 2009.

69 YING, Ding et al. Raman tensor of layered WS_2. **SCIENCE CHINA Materials**.

70 TONNDORF, Philipp et al. Photoluminescence emission and Raman response of monolayer MoS_2, $MoSe_2$, and WSe_2. **Optics express**, v.

21, n. 4, p. 4908-4916, 2013.

71 LIN, Zhong et al. Defect engineering of two-dimensional transition metal dichalcogenides. **2D Materials**, v. 3, n. 2, p. 022002, 2016.

72 MEYER, Ernst; HUG, Hans J.; BENNEWITZ, Roland. **Scanning probe microscopy: the lab on a tip**. Springer Science & Business Media, 2003.

73 VOIGTLÄNDER, Bert. **Scanning probe microscopy: Atomic force microscopy and scanning tunneling microscopy**. Springer, 2015.

74 DA COSTA, Marcelo Eduardo Huguenin Maia. **Síntese e caracterização estrutural do grafeno sobre Ge (100) obtido por deposição química na fase vapor**. 2018. Tese de Doutorado. PUC-Rio.

75 BARBOSA, A. N. et al. Direct synthesis of bilayer graphene on silicon dioxide substrates. **Diamond and Related Materials**, v. 95, p. 71-76, 2019.

76 JO, Sanghyun et al. Mono-and bilayer WS2 light-emitting transistors. **Nano letters**, v. 14, n. 4, p. 2019-2025, 2014.

77 HE, Zhengyu et al. Revealing defect-state photoluminescence in monolayer WS_2 by cryogenic laser processing. **ACS nano**, v. 10, n. 6, p. 5847-5855, 2016.

78 LI, Hong et al. From bulk to monolayer MoS_2: evolution of Raman scattering. **Advanced Functional Materials**, v. 22, n. 7, p. 1385-1390, 2012.

79 SCHEUSCHNER, Nils et al. Resonant Raman profiles and μ-photoluminescence of atomically thin layers of molybdenum disulfide. **Physica status solidi (b)**, v. 249, n. 12, p. 2644-2647, 2012.

80 STAIGER, Matthias et al. Splitting of monolayer out-of-plane A 1′ Raman mode in few-layer WS_2. **Physical Review B**, v. 91, n. 19, p.

195419, 2015.

81 SONG, Q. J. et al. Physical origin of Davydov splitting and resonant Raman spectroscopy of Davydov components in multilayer $MoTe_2$. **Physical Review B**, v. 93, n. 11, p. 115409, 2016.

82 FROEHLICHER, Guillaume et al. Unified description of the optical phonon modes in N-layer $MoTe_2$. **Nano letters**, v. 15, n. 10, p. 6481-6489, 2015.

83 KIM, Kangwon et al. Davydov splitting and excitonic resonance effects in Raman spectra of few-layer $MoSe_2$. **ACS nano**, v. 10, n. 8, p. 8113-8120, 2016.

84 ATKINS, Peter W.; FRIEDMAN, Ronald S. **Molecular quantum mechanics**. Oxford university press, 2011.

85 VAN DER HEIDE, Paul. **X-ray photoelectron spectroscopy: an introduction to principles and practices**. John Wiley & Sons, 2011.

86 CARUSO, Francisco; OGURI, Vitor. **Física Moderna: origens clássicas e fundamentos quânticos**. Elsevier, 2006.

87 MENDES, F. M. T. Introdução à Técnica de Espectroscopia Fotoeletrônica por raios X (XPS). **Synergia: FAPERJ**, 2011.

88 SHI, Wei et al. Raman and photoluminescence spectra of two-dimensional nanocrystallites of monolayer WS_2 and WSe_2. **2D Materials**, v. 3, n. 2, p. 025016, 2016.

89 ZHU, Yao et al. Scalable synthesis and defect modulation of large monolayer WS_2 via annealing in H_2S atmosphere/thiol treatment to enhance photoluminescence. **Applied Surface Science**, v. 485, p. 101-107, 2019.

90 DEL CORRO, Elena et al. Atypical exciton–phonon interactions in WS_2 and WSe_2 monolayers revealed by resonance Raman spectroscopy. **Nano letters**, v. 16, n. 4, p. 2363-2368, 2016.

91 BERKDEMIR, Ayse et al. Identification of individual and few layers of WS_2 using Raman Spectroscopy. **Scientific reports**, v. 3, n. 1, p. 1-8, 2013.

92 DEFO, Rodrick Kuate et al. Strain dependence of band gaps and exciton energies in pure and mixed transition-metal dichalcogenides. **Physical Review B**, v. 94, n. 15, p. 155310, 2016.

93 YAO, Huizhen et al. Significant photoluminescence enhancement in WS_2 monolayers through Na_2S treatment. **Nanoscale**, v. 10, n. 13, p. 6105-6112, 2018.

94 KWON, Yongjae et al. Variation of photoluminescence spectral line shape of monolayer WS_2. **Current Applied Physics**, v. 18, n. 8, p. 941-945, 2018.

95 AZCATL, Angelica et al. Covalent nitrogen doping and compressive strain in $MoS_2$by remote N_2 plasma exposure. **Nano letters**, v. 16, n. 9, p. 5437-5443, 2016.

96 MEISL, G. et al. Implantation and erosion of nitrogen in tungsten. **New journal of physics**, v. 16, n. 9, p. 093018, 2014.

97 TANG, Baoshan et al. Direct n-to p-type channel conversion in monolayer/few-layer WS_2 field-effect transistors by atomic nitrogen treatment. **ACS nano**, v. 12, n. 3, p. 2506-2513, 2018.

98 AYALA, Paola et al. Tailoring N-doped single and double wall carbon nanotubes from a nondiluted carbon/nitrogen feedstock. **The Journal of Physical Chemistry C**, v. 111, n. 7, p. 2879-2884, 2007.

99 SHALLENBERGER, J. R.; COLE, D. A.; NOVAK, S. W. Characterization of silicon oxynitride thin films by x-ray photoelectron spectroscopy. **Journal of Vacuum Science & Technology A: Vacuum, Surfaces, and Films**, v. 17, n. 4, p. 1086-1090, 1999.

7
Appendix: Published articles as a Ph.D. student.

[1] BARBOSA, A.N.; MENDOZA, C.D.; LEI, Y.; GIAROLA, M.; TERRONES, M.; MARIOTTO, G.; FREIRE, F.L. Photoluminescence modulation of CVD grown WS2 monolayers treated with low-power Ar Plasma. Materials Chemistry and Physics. (Submitted).

Abstract:

One of the main aspects of transition metal dichalcogenides (TMDs) is the possibility of light emission due to its indirect-to-direct bandgap transition when one isolates into a single layer. The introduction of defects in such materials is of great importance to further understand the reliability of TMDs as candidates for a low-power luminescent device basis. Herein, monolayer WS2 was synthesized by chemical vapor deposition and then subjected to Ar plasma treatment. The property change was monitored using Raman spectroscopy, photoluminescence spectroscopy, X-ray photoelectron spectroscopy, and atomic force microscopy. We show the influence of defects in the intensity of the PL signal and a redshift due to an increase in the defect density, introduced by increasing the plasma treatment time.

[2] BARBOSA, A.N.; MENDOZA, C.D.; FIGUEROA, N.S.J.; TERRONES, M.; FREIRE, F.L. Luminescence enhancement and Raman characterization of defects in WS2 monolayers treated with low-power N2 Plasma. APPLIED SURFACE SCIENCE, v. 534, p. 147685, 2020.

Abstract:

In this work, WS2 monolayers synthesized by chemical vapor deposition were submitted to low-power N2 plasma treatment for different periods of exposition, and its properties were studied by using a multi-technique approach. The results show that the photoluminescence signal from WS2 monolayers gradually increases for short treatment times and quenches for longer periods of

plasma exposure. Raman spectra of the treated WS2 monolayers also show that the E2g/ and A1g peak positions did not change significantly, suggesting that the treatment is not imposing a significant mechanical strain or substantial lattice deformation. X-ray photoelectron spectroscopy (XPS) revealed the presence of N impurities incorporated into the lattice, while AFM confirms that for short treatment times, the sample keeps its integrity. Our results suggested that low-energy cold plasma treatment can be a reliable way to control WS2 optoelectronic properties.

[3] BARBOSA, A.N.; FIGUEROA, N.S.; GIAROLA, M.; MARIOTTO, G.; FREIRE, F.L. Straightforward identification of monolayer WS2 structures by Raman spectroscopy. MATERIALS CHEMISTRY AND PHYSICS, v. 243, p. 122599, 2020.

Abstract:

Tungsten disulfide (WS2) is a very promising material with great potential for optoelectronics applications. To grow WS2 monolayer samples, chemical vapor deposition (CVD) is reliable for controlling the sample quality. However, there is still a lot of debate on whether the method is controllable beyond research-only systems. Although monolayer crystals are prepared through CVD, the challenge is to efficiently characterize and differentiate monolayer crystals from bilayers and a few-layers. In this work, we report a new straightforward Raman peak identification to discriminate monolayer WS2 crystals from layered and bulk samples. Our method is based on the A1g peak behavior. We show that through the comparison and analysis of other less convenient techniques that the strong splitting in A1g mode in close-to-resonance excitation energy condition is a much more convenient and fast identification method than either low-wavenumber Raman scattering characterization or atomic force microscopy.

[4] AMARAL CARMINATI, SAULO; **DO NASCIMENTO BARBOSA, ANDRÉ**; LUIZ MARTINS DE FREITAS, ANDRE; FREIRE, FERNANDO LÁZARO; SOUZA, FLÁVIO LEANDRO; NOGUEIRA, ANA FLÁVIA. Unraveling the role of single-layer graphene as an overlayer on hematite photoanodes. JOURNAL OF CATALYSIS, v. 372, p. 109-118, 2019.

Abstract:

In this work, the role of the single-layer graphene as an overlayer on the hematite photoanodes surface was investigated for water oxidation reaction via the photoelectrochemical process. Single-layer graphene (SLG) was synthesized by chemical vapor deposition (CVD) and transferred from the copper foil to the α-Fe2O3 photoanode surface. To ensure the purity and quality of SLG, the elemental composition of the samples was investigated in all steps, and no metal (Cu) trace was found after the transference onto the photoanode surface. The photocurrent density of α-Fe2O3/graphene photoanode was increased from 1.25 to 1.64 mA cm−2 at 1.23 VRHE compared to bare α-Fe2O3 photoanode. The role of SLG added on α-Fe2O3, and the charge carrier dynamics were investigated combining transient absorption spectroscopy (TAS) and surface photovoltage spectroscopy (SPS). These combined techniques revealed that the photogenerated holes had their lifetime increased due to applied bias and after the SLG deposition onto the α-Fe2O3 photoanode surface. Consequently, the photochemical separation and transfer of the photogenerated charge carriers became more efficient in the presence of SLG. The incorporation of SLG on the α-Fe2O3 photoanode is believed to suppress the surface traps, enabling holes to diffuse into the solid-liquid interface and promoting water oxidation reaction driven by sunlight irradiation.

[5] NASCIMENTO BARBOSA, ANDRÉ DO; ROMANI, E.C.; MENDOZA, C.D.; MAIA DA COSTA, M.E.H.; FREIRE, F.L. Direct synthesis, and characterization of graphene layers on silica glass substrates. MATERIALS TODAY: PROCEEDINGS, v. 10, p. 400-407, 2019.

Abstract:

The direct synthesis of graphene on semiconductors and dielectric substrates is of high interest. This process bypasses typical transfer procedures, which usually use polymers as sacrifice layers and toxic chemicals, and it leaves out residues and often damages the graphene flakes. The interest of direct graphene synthesis comes as high yield; electronic-grade graphene is only possible by eliminating the transfer process and tuning the growth process to maximize graphene quality. The graphene layers were synthesized on silica glass substrates by chemical vapor deposition at a semi-atmospheric pressure

environment inside the tube reactor, using controlled mixtures of hydrogen, argon, and methane gases. The effects of the methane flux and the total pressure on the homogeneity of the graphene layers were investigated. The samples were characterized using Raman scattering spectroscopy and Raman mapping, X-ray photoelectron spectroscopy, and optical transmittance measurements. The last technique was used to determine the number of graphene layers in the samples. Large area, homogeneous bilayer graphene was obtained for an appropriate gas mixture, and Raman spectroscopy results indicate that misoriented graphene bilayers were obtained.

[6] BARBOSA, A.N.; PTAK, F.; MENDOZA, C.D.; MAIA DA COSTA, M.E.H.; FREIRE JR, F.L. Direct synthesis of bilayer graphene on silicon dioxide substrates. DIAMOND AND RELATED MATERIALS, v. 95, p. 71-76, 2019.

Abstract:

Graphene layers were synthesized on silica and 90, 300, 400, and 700 nm thick silicon dioxide films by chemical vapor deposition at semi-atmospheric pressure environment, using controlled mixtures of hydrogen, argon, and methane gases. The effects of the methane flux and the total pressure on the homogeneity of the graphene layers were investigated. The samples were characterized by Raman spectroscopy and mapping, X-ray photoelectron spectroscopy, and optical transmittance measurements. The latter method was used to determine the number of graphene layers of the samples. Scanning electron microscopy, atomic force microscopy was carried out to study the surface uniformity, and electrical measurements were also performed. Our results indicate that large area, a homogeneous nanocrystalline graphene layer, can be obtained with an appropriate choice of synthesis parameters. Raman spectroscopy results indicate turbostratic graphene bilayers were obtained.

[7] BARBOSA, ANDRÉ DO NASCIMENTO; FIGUEROA, N.J.S.; MENDOZA, C.D.; PINTO, A.L.; FREIRE, F.L. Characterization of graphene synthesized by low-pressure chemical vapor deposition using N-Octane as precursor. MATERIALS CHEMISTRY AND PHYSICS, v. 219, p. 189-195, 2018.

Abstract:

Chapter 7. Appendix

We report single-layer graphene synthesis using high-carbon content N-Octane as a precursor. Unlike methanol, ethanol, and other liquid carbon precursors, N-Octane is oxygen-free, and its molecular structure is simply a common hydrocarbon. The optimal precursor pressure for synthesis was found to be at 5–20 mTorr range. At higher partial pressures, we have achieved bilayer and few-layer coverage of the copper substrates with {111} plane parallel to the surface, as revealed by Raman spectroscopy. We could lower the synthesis temperature down to 850 °C and still obtained graphene layers with a low concentration of defects. For the complete coverage of the substrates, we report shorter than usual synthesis time, of no more than 5 min. Characterization of graphene layers was performed using Raman scattering spectroscopy and mapping, UV–vis transmittance as well as atomic force microscopy, scanning tunneling microscopy and scanning tunneling spectroscopy.